ADVANCED MATERIALS
www.advmat.de

Senescence Reprogramming Unleashes Tumor Immune Surveillance via Coordinated Gene Modulation

*Kai Zhao, Yu Yan, Bao-Ting Dong, Shan-Shan Pan, and Xian-Zheng Zhang**

Cellular senescence can recruit immune cells for tumor therapy through the senescence-associated secretory phenotype (SASP). However, its therapeutic efficacy is limited by immune tolerance and the immunosuppressive tumor microenvironment (TME). Reprogramming tumor-specific senescence through coordinated modulation of $P16^{INK4a}$ and PD-L1 enhances tumor immunogenicity and alleviates immunosuppression. To achieve this, a target-enhanced gene delivery nanoparticle is engineered using the urokinase plasminogen activator receptor (uPAR) as a senescence-specific targeting ligand, combined with a telomerase reverse transcriptase (TERT) promoter and a nuclear localization signal-microtubule-associated sequence (NLS-MTAS) peptide. This system efficiently induces tumor-specific senescence through cell-cycle arrest and promotes the chemotactic recruitment of cytotoxic immune cells. In vivo, the nanoparticle induces a robust anti-tumor response without causing systemic toxicity and significantly enhances the therapeutic efficacy of αCTLA-4 immune checkpoint blockade in subcutaneous, lung metastasis, postoperative recurrence, and spontaneous tumor models. This study emphasizes the therapeutic potential of reprogramming tumor-specific senescence to improve targeted gene delivery and immunotherapy outcomes, offering a viable approach for the treatment of immunologically "cold" tumors.

1. Introduction

$P16^{INK4a}$, which is encoded by the *CDKN2A* gene, is a critical tumor suppressor that regulates the cell cycle progression by inhibiting cyclin-dependent kinases 4 and 6 (CDK4/6), thereby preventing uncontrolled proliferation.[1] $P16^{INK4a}$ expression is strongly associated with cellular senescence, which is characterized by irreversible cell cycle arrest and a pro-inflammatory secretory profile known as the senescence-associated secretory phenotype (SASP).[2,3] The SASP recruits immune cells such as T cells and natural killer (NK) cells to facilitate the clearance of senescent and potentially tumorigenic cells.[4–7] Senescent tumor cells also enhance antigen presentation, boosting immunogenicity and eliciting adaptive anti-tumor responses.[8] However, chronic SASP-driven inflammation can promote immunosuppression in the tumor microenvironment (TME) by upregulating programmed death ligand 1 (PD-L1), which contributes to immune tolerance and evasion.[9–11] Furthermore, $P16^{INK4a}$-positive senescent cells stabilize PD-L1 through reduced ubiquitination and proteasomal degradation, thereby facilitating immune escape.[12,13]

Therapy-induced senescence (TIS) has emerged as a strategy to enhance antitumor immunity.[4] Combinations of senescence inducers with MAPK/ERK kinase inhibitors, retinoic acid receptor agonists, and other modulators have shown promise.[14–16] However, prolonged exposure to senescence can lead to T cell exhaustion, limiting the effectiveness of immune responses.[10,17,18] Although combining senescence inducers with immune checkpoint inhibitors shows promise, non-specific distribution can blunt the synergistic effects and impair immune cells by inducing undesired senescence.[19–22] Targeted nanocarriers that co-deliver senescence and immune modulators have been developed,[23–25] but their transient activity requires repeated dosing, which can lead to tumor resistance.[26]

Gene therapy enables the sustained production of therapeutic molecules in vivo, supporting long-term disease control and reducing the need for frequent dosing.[27,28] The programmability of gene therapy allows for the incorporation of tumor-specific promoters, such as the telomerase reverse transcriptase (TERT) and survivin promoters, to selectively express genes in tumor cells.[29,30] Furthermore, chimeric peptides that incorporate nuclear localization signals (NLS) and microtubule-associated sequences (MTAS) (NLS-MTAS) have been designed to mimic microtubule-based transport mechanisms observed in stem cells.[31] This strategy enables the efficient intracellular trafficking and nuclear delivery of gene therapeutics for cancer treatment. Notably, the urokinase plasminogen activator receptor (uPAR) is selectively overexpressed on senescent cells. Chimeric antigen receptor (CAR) and engineered peptides targeting uPAR have selectively eliminated senescent cells, establishing uPAR as a promising target for precision therapeutic delivery.[32–34]

K. Zhao, Y. Yan, B.-T. Dong, S.-S. Pan, X.-Z. Zhang
Department of Chemistry, Department of Traditional Chinese Medicine of Zhongnan Hospital, Key Laboratory of Biomedical Polymers of Ministry of Education
Wuhan University
Wuhan 430072, P.R. China
E-mail: xz-zhang@whu.edu.cn

The ORCID identification number(s) for the author(s) of this article can be found under https://doi.org/10.1002/adma.202516597

DOI: 10.1002/adma.202516597

In this study, we demonstrated that overexpression of $P16^{INK4a}$ in murine models of triple-negative breast cancer (TNBC) and colorectal cancer (CRC) significantly enhanced tumor immunogenicity and promoted the secretion of SASP factors. Concurrently, downregulation of PD-L1 expression effectively mitigated the immunosuppression associated with senescence-related immune tolerance, facilitating enhanced T cell recruitment and cytotoxicity. Based on these findings, we developed a uPAR-targeted gene delivery nanoparticle to co-modulate the expression of $P16^{INK4a}$ and PD-L1 using a multifunctional plasmid containing the TERT promoter, $P16^{INK4a}$ cDNA, a short hairpin RNA (shRNA) targeting PD-L1, and ZsGreen as a reporter gene in TNBC and CRC models. Specifically, a nanocomplex (PP) was formed from poly(β-amino ester) (PBAE), PBAE conjugated with an NLS-MTAS peptide (PBAE-NLS-MTAS), and plasmid DNA. Then, the surface of PP was functionalized with an optimized ratio of chondroitin sulfate (CS) and a uPAR antibody-CS conjugate (Ab-CS). This assembly constituted a target-enhanced gene delivery nanoparticle, termed TEPP (**Figure 1a**). TEPP demonstrated improved cellular uptake in senescent tumor cells, effective tumor-specific accumulation, and selective gene expression after systemic administration in mice. As a result, TEPP effectively modulated the expression of $P16^{INK4a}$ and PD-L1 in subcutaneous, lung metastasis, postoperative recurrence, and spontaneous tumor models. This modulation reactivated immune surveillance in immunologically "cold" tumors and significantly enhanced the efficacy of immune checkpoint blockade (ICB) therapy, leading to substantial inhibition of tumor growth and metastasis. In conclusion, this study presents a gene delivery nanoparticle designed to induce tumor-specific senescence reprogramming, thereby improving targeted delivery and immune activation. These results suggest that gene nanomedicine is a promising strategy for senescence-based cancer immunotherapy in clinical settings.

2. Results and Discussion

2.1. Overexpression of $P16^{INK4a}$ Enhances Tumor Immunogenicity and Facilitates Immune Infiltration via the SASP

We first investigated the impact of gene mutations on patient survival in immunologically "cold" tumors, specifically BRCA and CRC. Notably, mutations in the *CDKN2A* gene, which encodes the tumor suppressor protein $P16^{INK4a}$, were associated with significantly reduced overall survival compared to the wild-type genotype (Figure 1b,c and Figure S1, Supporting Information). Additionally, low expression levels of $P16^{INK4a}$ have been strongly correlated with poor prognosis in solid tumors.[35,36] To explore the phenotypic consequences of $P16^{INK4a}$ overexpression, we used 4T1 and CT26 murine cell lines. Western blot analysis confirmed the expression of retinoblastoma protein (Rb), a downstream target of CDK4/6, in both cell lines (Figure S2, Supporting Information). $P16^{INK4a}$ overexpression induced a senescent phenotype, as evidenced by increased senescence-associated β-galactosidase (SA-β-gal) staining (Figure 1d), enlarged cell morphology (Figure 1e), decreased Ki67 expression, and elevated P21 levels (Figure 1f). These changes were accompanied by a significant decrease in cell proliferation, nearly reaching complete growth arrest compared to control cells (Figure S3, Supporting Information). Furthermore, $P16^{INK4a}$ overexpression significantly increased the surface expression of the antigen-presenting molecule MHC-I (Figure 1f), as confirmed by flow cytometry (FCM) analysis (Figure S4a, Supporting Information). Similar phenotypic alterations were observed in CT26 cells (Figures S4b and S5, Supporting Information), suggesting that $P16^{INK4a}$ overexpression enhances the immunogenicity of tumor cells. To investigate the transcriptional effects of $P16^{INK4a}$ overexpression, we performed quantitative real-time PCR (qRT-PCR). The results showed significant upregulation of genes associated with antigen presentation, including *H2-K1*, *Nlrc5*, and *Tap1*, as well as pro-inflammatory and chemotactic cytokines such as *Il1β*, *Il6*, *Il8*, *Ccl5*, and *Cxcl10* (Figure 1g). ELISA analysis of culture supernatants from $P16^{INK4a}$-overexpressing 4T1 cells revealed significantly elevated levels of pro-inflammatory cytokines, including IL-6, and CCL5 and CXCL10, compared to control cells (Figure 1h). These results were consistent with the SASP, wherein senescent cells secreted a variety of pro-inflammatory cytokines and chemokines.

To evaluate the effects of $P16^{INK4a}$ overexpression on the TME in vivo, we established a stable Tight-$P16^{INK4a}$ cell line with a Tet-on inducible system, allowing for the controlled expression of $P16^{INK4a}$ after doxycycline (Dox) administration. These cells were then subcutaneously implanted into BALB/c mice (Figure 1i). In vivo induction of $P16^{INK4a}$ significantly enhanced tumor immunogenicity compared to control tumors, as evidenced by elevated expression of MHC-I (Figure 1j). Furthermore, tumors with $P16^{INK4a}$ overexpression exhibited markedly increased infiltration of both $CD4^+$ and $CD8^+$ T cells at TNBC and CRC sites (Figure 1k), which may be driven by the chemotactic effects of SASP-associated pro-inflammatory factors.[37] Taken together, these results showed that $P16^{INK4a}$ overexpression enhanced tumor immunogenicity and promoted immune cell infiltration in TNBC and CRC tumors through SASP-mediated modulation of the TME, offering potential therapeutic avenues for enhancing anti-tumor immunity.

2.2. Coordinated Modulation of $P16^{INK4a}$ and PD-L1 Expression Effectively Overcomes Immunosuppression

Although overexpression of $P16^{INK4a}$ enhanced tumor immunogenicity through the SASP, it also upregulated PD-L1 expression at both transcriptional and protein levels, which could lead to immune tolerance (Figure 1g and Figure S6a, Supporting Information). FCM analyses confirmed a significant increase in surface PD-L1 expression on $P16^{INK4a}$-overexpressing tumor cells (Figure S6b,c, Supporting Information). Notably, PD-L1 showed the most significant upregulation compared to other commonly studied immunosuppressive receptors (Figure S7, Supporting Information). To further investigate the relationship between antigen presentation and PD-L1 expression in tumors, $P16^{INK4a}$ was overexpressed in B16-OVA cells. The results showed that the proportion of $H\text{-}2K^b\text{-}SIINFEKL^+PD\text{-}L1^+$ cells increased markedly to 17.7% after $P16^{INK4a}$ overexpression, compared to 2.85% in the control group, indicating that enhanced antigen presentation was accompanied by elevated PD-L1 expression (Figure S8, Supporting Information). Further immunohistochemical analyses of tumor tissues revealed that PD-L1 expression increased

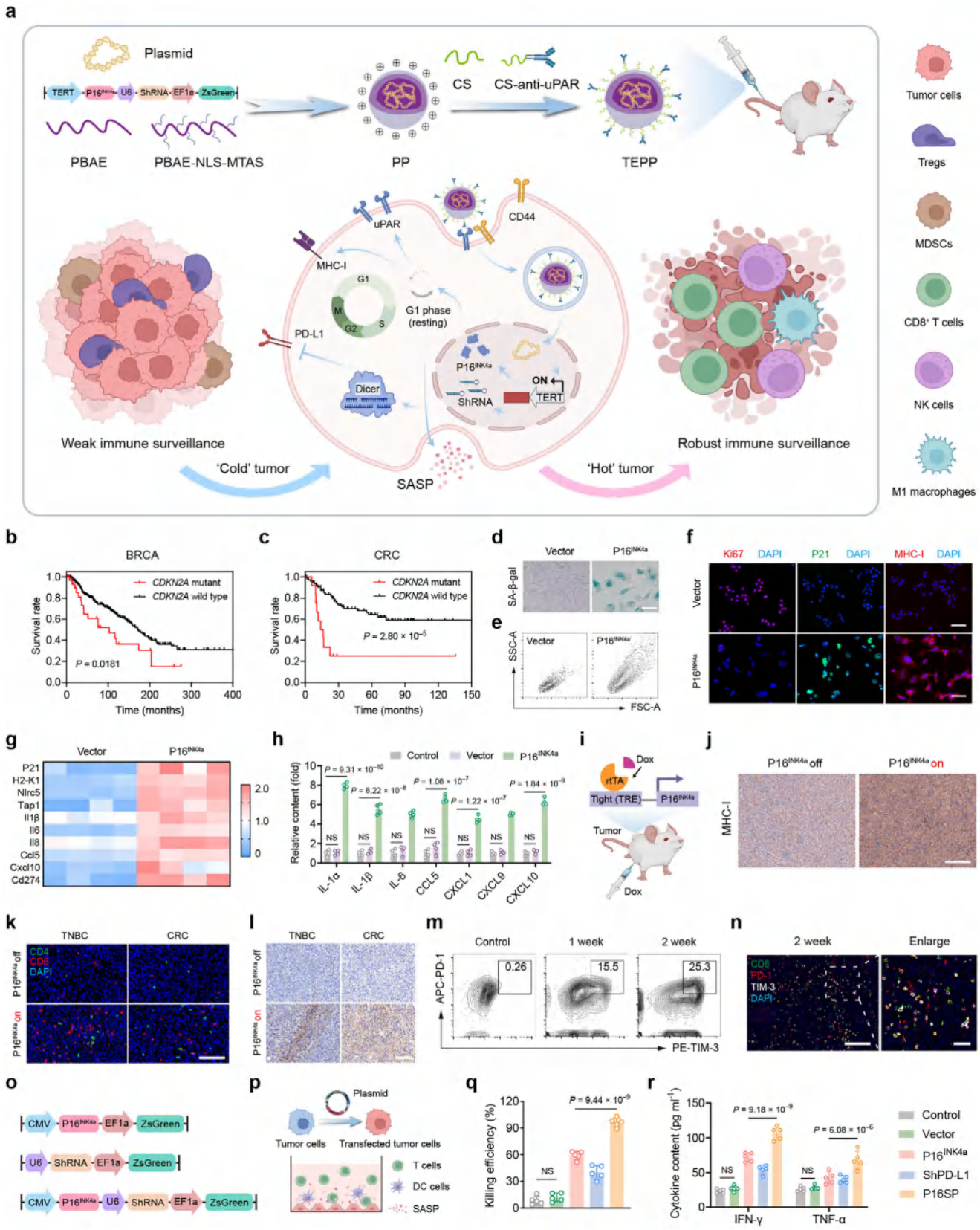

markedly in both TNBC and CRC tumor sites after P16^{INK4a} overexpression (Figure 1l). This upregulation may impair the cytotoxic activity of infiltrating immune cells, thereby limiting the anti-tumor response. FCM analyses and immunofluorescence staining showed a time-dependent increase in the proportion of exhausted CD8$^+$ T cells in tumors with sustained P16^{INK4a} overexpression (Figure 1m,n), suggesting that while P16^{INK4a} overexpression enhanced immune cell recruitment via SASP, concurrent PD-L1 induction may contribute to T cell exhaustion and diminish their tumor-killing capacity.

To enhance P16^{INK4a} expression and suppress PD-L1-mediated immunosuppression at the tumor site simultaneously, we engineered a dual-function plasmid (pP16SP) that co-expressed P16^{INK4a} and encoded a shRNA targeting PD-L1 for knockdown. Single-expression plasmids and an empty vector were used as controls (Figure 1o). 4T1 cells stably transfected with either the control plasmid or the pP16SP plasmid were co-cultured with murine splenocytes to evaluate immune-mediated cytotoxicity (Figure 1p). Lactate dehydrogenase (LDH) assays showed that pP16SP significantly increased immune cell-mediated tumor cell killing, achieving 96.31% cytotoxicity compared to 12.09% in the vector group (Figure 1q). This effect was attributed to improved antigen presentation and SASP-induced activation of cytotoxic immune cells. Furthermore, elevated levels of IFN-γ and TNF-α in the culture supernatant confirmed that pP16SP effectively alleviated immunosuppression and activated T cell responses (Figure 1r). Taken together, these results showed that the pP16SP transfection enhanced tumor immunogenicity and immune cell recruitment through P16^{INK4a} overexpression while concurrently mitigating immune suppression via PD-L1 knockdown, thereby potentiating anti-tumor immune responses.

2.3. Development and Characterization of the uPAR-Targeted Nanoparticle TEPP

Recent studies have identified elevated uPAR expression as a hallmark of senescent cells.[32] To investigate the impact of P16^{INK4a} overexpression on uPAR expression, we conducted comprehensive in vitro and in vivo analyses. FCM analyses showed a significant increase in uPAR surface expression in 4T1 cells with P16^{INK4a} overexpression, with the proportion of uPAR-positive cells rising from 6.39% in the vector control group to 43.6% in the P16^{INK4a} overexpression group (**Figure 2**a,b). qRT-PCR revealed a 1.87-fold increase in uPAR mRNA levels compared to control cells (Figure 2c). Fluorescence in situ hybridization (FISH) further confirmed increased uPAR localization on the cell surface in cells transfected with pP16^{INK4a}-EGFP (Figure 2d). Consistently, in vivo induction of P16^{INK4a} led to a marked increase in uPAR expression in tumor tissues (Figure 2e). These results showed that uPAR was significantly upregulated in response to P16^{INK4a} overexpression, positioning it as a viable target for tumor-specific therapeutic delivery.

For tumor-targeted gene delivery, we selected poly(β-amino ester) (PBAE) and PBAE-NLS-MTAS polymers as core carriers, leveraging PBAE's biodegradability and the NLS-MTAS peptide's microtubule-targeting capability. The successful synthesis of the NLS-MTAS peptide was confirmed by electrospray ionization mass spectrometry (ESI-MS) (Figure S9, Supporting Information). Proton nuclear magnetic resonance (^{1}H-NMR) spectroscopy and gel permeation chromatography (GPC) analyses confirmed the successful synthesis of PBAE and its subsequent modification with the NLS-MTAS peptide (Figure S10 and S11, Supporting Information). Fourier-transform infrared (FTIR) spectroscopy showed a distinct amide band at 1678 cm^{-1}, confirming the conjugation of PBAE with the NLS-MTAS peptide (Figure S12, Supporting Information). Gel electrophoresis and transfection efficiency assays determined an optimal polymer-to-plasmid weight ratio of 45:1 (Figure S13, Supporting Information). Confocal laser scanning microscopy (CLSM) and FCM analyses further confirmed that the incorporation of the NLS-MTAS peptide significantly enhanced plasmid nuclear entry and improved transfection efficiency (Figure S14, Supporting Information). CS was selected as a coating material due to its natural affinity for CD44 receptors, which were commonly overexpressed on tumor cell surfaces.[38] To improve tumor targeting by taking advantage of uPAR upregulation, an anti-uPAR antibody was conjugated to CS through an amide coupling reaction to form Ab-CS. The successful synthesis of Ab-CS was confirmed by ^{1}H-NMR analysis (Figure S15, Supporting Information). Various ratios of CS and Ab-CS were applied to the nanocomplex surface, with uncoated and single-coated formulations serving as controls. Cellular uptake studies in 4T1-Vector and 4T1-P16^{INK4a} cells revealed that a 1:1 CS/Ab-CS coating ratio exhibited

Figure 1. Coordinated modulation of P16^{INK4a} and PD-L1 enhances tumor immune surveillance. a) Schematic illustration of the TEPP system design and its mechanism of action in mediating senescence-induced immunotherapy through enhanced tumor targeting and selective gene expression. b,c) Correlation between *CDKN2A* mutation status and overall survival in patients with BRCA (b) and CRC (c), analyzed using cBioPortal. d) Representative images of SA-β-gal staining and e) FCM analysis of 4T1-Vector and 4T1-P16^{INK4a} cells. Scale bar: 50 µm. f) Representative immunofluorescence staining of Ki67, P21, and MHC-I in 4T1-Vector and 4T1-P16^{INK4a} cells. Scale bar: 50 µm. g) qRT-PCR analysis of mRNA expression for senescence marker (*P21*), antigen presentation-related genes (*H2-K1*, *Nlrc5*, *Tap1*), SASP-associated cytokines (*Il1β*, *Il6*, *Il8*, *Ccl5*, *Cxcl10*), and *Cd274* in 4T1-Vector and 4T1-P16^{INK4a} cells. Data shown as heat maps (n = 4 independent samples). h) ELISA quantification of SASP factors (IL-1α, IL-1β, IL-6, CCL5, CXCL1, CXCL9, and CXCL10) in the culture supernatants of 4T1, 4T1-Vector, and 4T1-P16^{INK4a} cells (n = 4). i) Schematic of Dox administration in tumor-bearing mice inoculated with Tight-P16^{INK4a} cells to induce P16^{INK4a} expression. j) Representative immunohistochemical staining of MHC-I in TNBC tissues without or with Dox-induced P16^{INK4a} expression. Scale bar: 100 µm. k) Representative immunofluorescence staining of CD4 and CD8, and l) immunohistochemical staining of PD-L1 in TNBC and CRC tissues with or without P16^{INK4a} expression. Scale bar: 100 µm. m) Representative FCM plots of exhausted CD8$^+$ T cells (PD-1$^+$TIM-3$^+$ among CD8$^+$) in TNBC tissues without Dox treatment and after 1 or 2 weeks of Dox-induced P16^{INK4a} expression. n) Representative immunofluorescence staining of CD8, PD-1, and TIM-3 in TNBC tissues after 2 weeks of Dox-induced P16^{INK4a} expression. Scale bar: 200 µm (inset: 50 µm). o) Schematic diagrams of plasmids used for P16^{INK4a} expression, PD-L1-targeting shRNA, and co-regulatory constructs. p) Schematic illustration of co-incubation of transfected tumor cells with whole spleen cells. q-r) After 24 h of co-culture, tumor cell killing efficiency was measured by LDH release q), and IFN-γ and TNF-α levels in the supernatant were quantified by ELISA r) (n = 5). Data in (h,q,r) are presented as mean ± s.d. *P* values were calculated by log-rank (Mantel-Cox) test (b,c), two-way ANOVA with Tukey's post hoc correction (h,r), or one-way ANOVA with Tukey's post hoc correction (q).

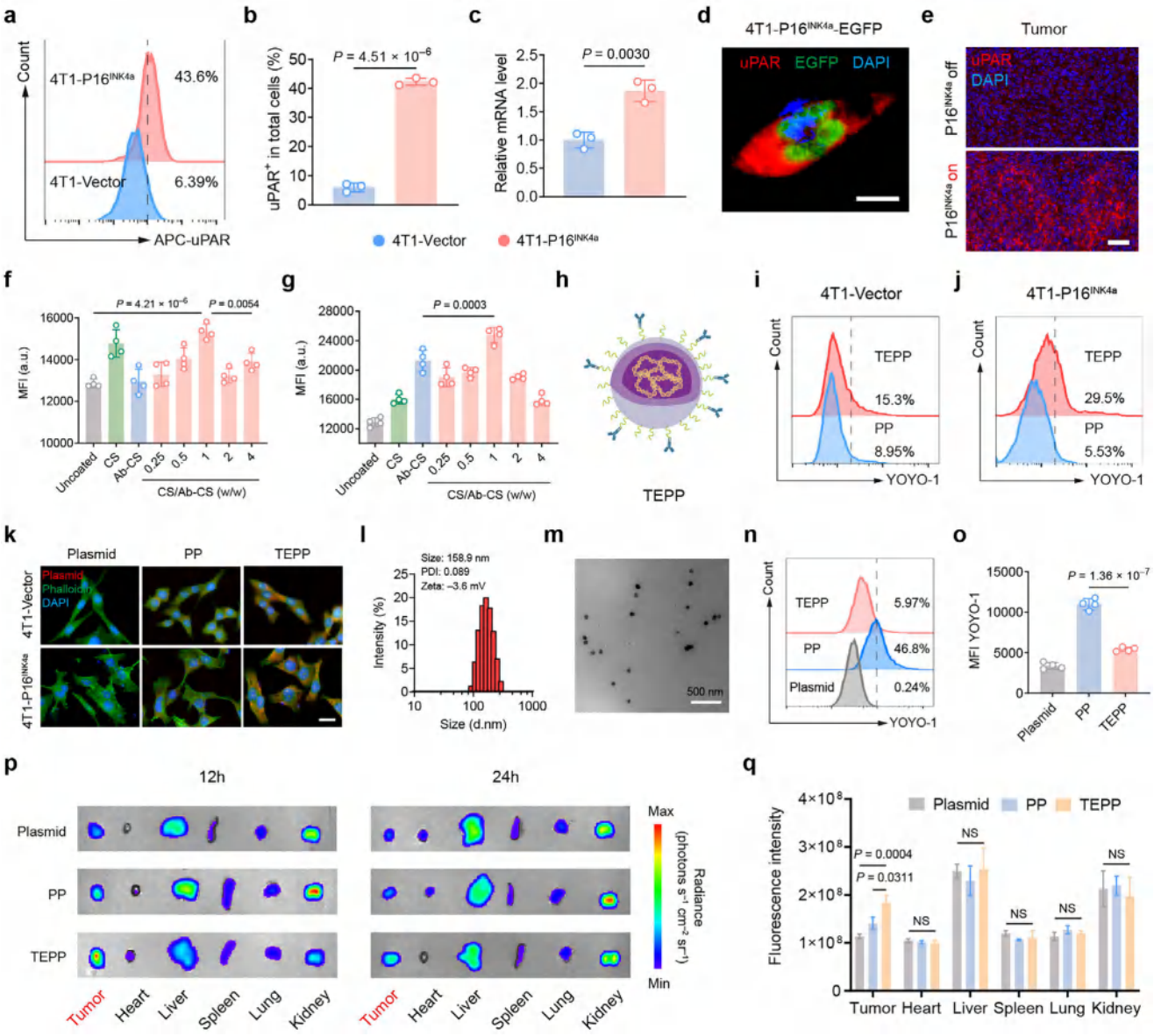

Figure 2. Identification of uPAR as a target and construction of the TEPP system. a) Representative FCM plots, b) corresponding quantitative analysis of uPAR surface expression, and c) qRT-PCR analysis of *Plaur* mRNA levels in 4T1-Vector and 4T1-P16^{INK4a} cells. d) FISH imaging of uPAR expression in 4T1-P16^{INK4a}-EGFP cells, where EGFP fluorescence indicates plasmid expression. Scale bar: 20 µm. e) FISH analysis of uPAR expression in TNBC tissues with or without Dox-induced P16^{INK4a} expression. Scale bar: 50 µm. f,g) Quantitative mean fluorescence intensity (MFI) analysis of endocytic efficiency for PP nanoparticles modified with varying ratios of CS and Ab-CS in 4T1-Vector (f) and 4T1-P16^{INK4a} (g) cells, determined by FCM. Plasmids were labeled with YOYO-1 dye (n = 4 independent samples). h) Schematic illustration of the TEPP nanoparticle architecture. i,j) Representative FCM plots showing the uptake of YOYO-1-labeled PP and TEPP nanoparticles by 4T1-Vector (i) and 4T1-P16^{INK4a} (j) cells. k) Representative CLSM images of cellular uptake of YOYO-3-labeled naked plasmids, PP, and TEPP nanoparticles in 4T1-Vector and 4T1-P16^{INK4a} cells. Scale bar: 20 µm. l) Size distribution profile and m) representative TEM image of TEPP nanoparticles. n) Representative FCM plots and o) quantitative analysis of cellular uptake of naked plasmids, PP, and TEPP nanoparticles by RAW264.7 macrophages (n = 4). p) Representative IVIS images of tumors and major organs from TNBC tumor-bearing mice at 12 and 24 h after intravenous injection of TOTO-3-labeled plasmids, PP, or TEPP nanoparticles. q) Quantitative fluorescence intensity in tumors and major organs at 24 h post-injection, corresponding to data in (p) (n = 3). Data in (b,c,f,g,o,q) are shown as mean ± s.d. P values were calculated by unpaired two-tailed Student's t-test (b,c), one-way ANOVA with Tukey's post hoc correction (f,g,o), or two-way ANOVA with Tukey's post hoc correction (q).

superior endocytosis efficiency in both cell types (Figure 2f,g), leading to the construction of the target-enhanced nanoparticle TEPP (Figure 2h). Under these conditions, the antibody conjugation efficiency was calculated to be 49.7%, and the average number of antibodies immobilized on each TEPP nanoparticle was approximately 212 (Figure S16, Supporting Information). Specifically, TEPP exhibited a 1.15-fold increase in uptake compared to PP in 4T1-Vector cells and a 2.28-fold increase in 4T1-P16^{INK4a} cells with elevated uPAR expression (Figure 2i,j and Figure S17, Supporting Information). CLSM imaging further corroborated these results, visually confirming enhanced cellular internalization (Figure 2k).

The average particle size of the TEPP was measured at 158.9 nm using dynamic light scattering. The TEPP had a polydispersity index of 0.089 and a zeta potential of −3.6 mV (Figure 2l). Transmission electron microscopy (TEM) imaging showed that the TEPP particles had a uniform and dense spherical morphology (Figure 2m). The PicoGreen assay demonstrated that TEPP exhibited a high plasmid encapsulation efficiency of 98.9%. Furthermore, plasmid release was significantly enhanced under acidic conditions relative to physiological pH (Figure S18, Supporting Information). Notably, TEPP exhibited long-term stability in serum-containing culture medium and effectively protected the encapsulated plasmid DNA from DNase I-mediated degradation (Figure S19, Supporting Information). Given that systemically administered nanoparticles were often recognized and cleared by macrophages, which substantially reduced their tumor accumulation.[39] We assessed the uptake of TEPP in RAW264.7 mouse macrophage cells. TEPP showed a significantly reduced uptake rate of 5.97% following surface coating modification, compared to an uptake rate of 46.8% for unmodified PP (Figure 2n,o). These results suggested that the applied coating effectively reduced macrophage-mediated clearance, thereby enhancing gene delivery efficiency at the tumor site.

To assess the in vivo biodistribution, TOTO-3-labeled plasmid, PP, and TEPP were intravenously administered to 4T1 tumor-bearing mice. The organ distribution was monitored at various time points by an in vivo imaging system (IVIS). At 12 h post-injection, TEPP exhibited significantly higher fluorescence intensity at the tumor site compared to both the PP and Plasmid groups. Although overall tumor-site fluorescence decreased by 24 h, the TEPP group maintained fluorescence intensities that were 1.62- and 1.31-fold higher than the plasmid and PP groups, respectively (Figure 2p,q). Notably, TEPP showed markedly improved transfection efficiency in tumor tissues compared to the other groups (Figure S20, Supporting Information). These results showed the strong tumor-targeting capability and effective gene delivery performance of TEPP after systemic administration.

2.4. TEPP$_{P16SP}$ Induces Cell Cycle Arrest and Immune Activation In Vitro

To evaluate the synergistic effects of modulating P16^{INK4a} overexpression and PD-L1 knockdown on tumor cell cycle regulation and immune activation, we encapsulated the pP16SP plasmid in TEPP nanoparticle (TEPP$_{P16SP}$). The control formulations included an empty vector (TEPP$_{Vector}$), a single-gene overexpression construct (TEPP$_{P16INK4a}$), and a PD-L1 knockdown construct (TEPP$_{ShPD-L1}$). FCM analysis showed that treatment with TEPP$_{P16SP}$ and TEPP$_{P16INK4a}$ significantly arrested tumor cells in the G1 phase (**Figure** 3a,b), which was attributed to CDK4/6 inhibition mediated by P16^{INK4a} overexpression. Notably, PD-L1 knockdown further enhanced this effect, likely by promoting cellular senescence,[40] thereby amplifying the regulatory efficacy of TEPP$_{P16SP}$. Immunostaining for the proliferation marker Ki67 and the senescence marker γH2A.X showed that tumor cells treated with TEPP$_{P16SP}$ exhibited a nearly complete loss of proliferative capacity and transitioned into a senescent state (Figure 3c). FCM analyses showed that TEPP$_{P16SP}$ treatment led to a significant increase in surface expression of MHC-I and a reduction in PD-L1 levels (Figure 3d,e and Figure S21, Supporting Information), indicating enhanced tumor immunogenicity and potential immune reactivation.

We further assessed the chemotactic response of T cells toward TEPP$_{P16SP}$-treated tumor cells using a transwell migration assay (Figure 3f). The results showed a 4.06-fold increase in T cell migration to the lower chamber compared to the control group (Figure 3g). Notably, the proportion of CD8$^+$ T cells increased to 10.56% in the TEPP$_{P16SP}$ group compared with 3.58% in the control group and 6.68% in the TEPP$_{P16INK4a}$ group (Figure 3h). Elevated levels of IFN-γ and TNF-α in the culture supernatant further confirmed robust T cell activation in response to TEPP$_{P16SP}$ treatment (Figure S22a, Supporting Information). To evaluate the cytotoxic activity, we monitored calcein leakage from tumor cells, which served as a direct indicator of T cell-mediated killing (Figure 3i). FCM analysis showed a significant reduction in calcein fluorescence in TEPP$_{P16SP}$-treated tumor cells, indicating enhanced T cell cytotoxicity (Figure 3j and Figure S22b, Supporting Information). In addition, LDH release assays showed that the efficiency of T cell-mediated tumor cell killing reached 72.42% in the TEPP$_{P16SP}$ group compared to 8.83% in the control group (Figure S22c, Supporting Information). Furthermore, CD8$^+$ T cells were isolated from OT-1 mice and co-cultured with B16-OVA cells following different treatments. The results demonstrated that TEPP$_{P16SP}$ treatment significantly enhanced the cytotoxic activity of T cells against tumor cells (Figure S23, Supporting Information). We also evaluated the ability of TEPP$_{P16SP}$-treated tumor cells to activate bone marrow-derived dendritic cells (BMDCs) (Figure 3k). FCM analysis showed that BMDC maturation reached 52.30% in the TEPP$_{P16SP}$ group, which was 2.39-fold and 2.16-fold higher than those in the control and TEPP$_{Vector}$ groups, respectively (Figure 3l,m). This enhanced activation is likely due to a strong SASP and reduced immunosuppressive signaling after TEPP$_{P16SP}$ treatment. Collectively, these results demonstrated that TEPP$_{P16SP}$ effectively promoted the recruitment and activation of both T cells and BMDCs in vitro by enhancing tumor immunogenicity and alleviating immunosuppressive mechanisms.

2.5. In Vivo Tumor-Specific Expression and Antitumor Efficacy of TEPP$_{P16SP}$

TERT is aberrantly overexpressed in most tumor types to regulate telomerase activity, while it is almost inactive in normal somatic tissues. Leveraging this tumor-specific expression pattern,

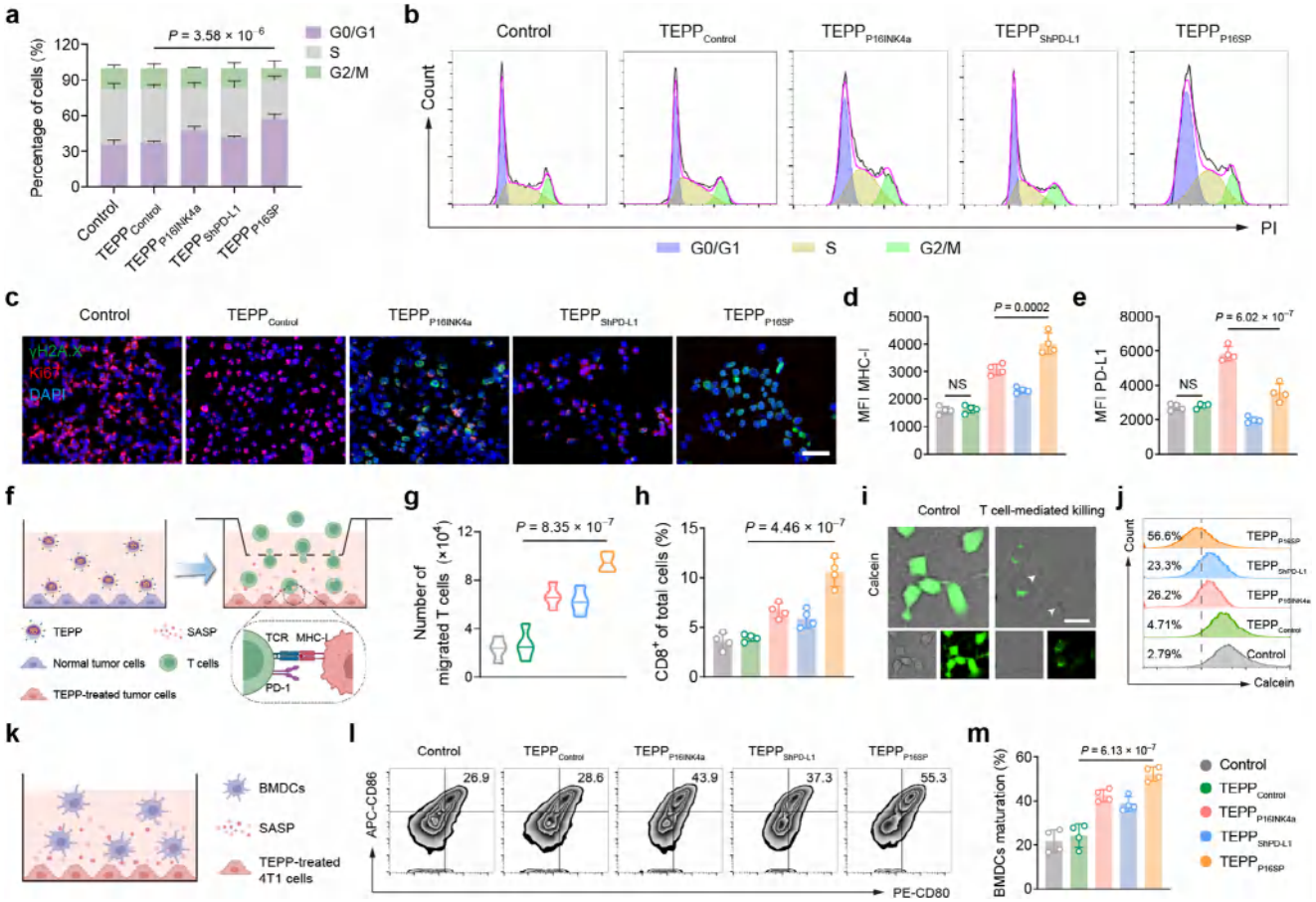

Figure 3. $TEPP_{P16SP}$ regulates cell cycle progression and promotes T cell recruitment and activation in vitro. a) Quantitative analysis of cell cycle distribution and b) representative FCM plots of 4T1 cells following different treatments (n = 3 independent experiments). c) Representative immunofluorescence staining of γH2A.X and Ki67 in treated 4T1 cells. Scale bar: 50 μm. d,e) Quantitative MFI analysis of MHC-I (d) and PD-L1 (e) surface expression in 4T1 cells after treatment, determined by FCM (n = 4 independent samples). f) Schematic illustration of the transwell chemotaxis assay used to assess T cell migration toward TEPP-treated 4T1 cells. T cells were isolated from the spleens of 4T1 tumor-bearing mice. g) Quantification of total chemotactic T cells migrating to the lower chamber and h) the proportion of $CD8^+$ T cells responding to differently treated 4T1 cells, analyzed by FCM (n = 4). i) Representative CLSM images showing calcein leakage from tumor cells, indicating T cell-mediated cytotoxicity. Scale bar: 20 μm. j) Representative FCM plots of calcein intensity in 4T1 cells after T cell co-culture under different treatment conditions. k) Schematic representation of co-culture experiments between TEPP-treated 4T1 cells and BMDCs. l) Representative FCM plots and m) corresponding quantitative analysis of BMDC maturation ($CD80^+CD86^+$) after 12 h co-culture with differently treated 4T1 cells (n = 4). Data in (a,d,e,g,h,m) are shown as mean ± s.d. P values were calculated using two-way ANOVA with Tukey's post hoc correction (a) or one-way ANOVA with Tukey's post hoc correction (d,e,g,h,m).

we incorporated the TERT promoter into the $TEPP_{P16SP}$ plasmid to enhance selective expression in tumor cells while minimizing off-target effects in normal tissues (**Figure** 4a). We first examined the promoter's selective activity in vitro by comparing its expression in tumor and non-malignant cell lines (Figure S24, Supporting Information). To further evaluate tumor-specific expression in vivo, 4T1 tumor-bearing mice were intravenously administered $TEPP_{P16SP}$ constructs driven by either the cytomegalovirus (CMV) promoter or the TERT promoter. Notably, the TERT promoter significantly enhanced $P16^{INK4a}$ expression in tumor tissues while minimizing expression in normal organs, especially the liver and lungs, compared to the CMV promoter (Figure 4b and Figure S25, Supporting Information). Furthermore, SA-β-gal staining confirmed that the TERT promoter selectively induced senescence in tumor tissues without affecting surrounding healthy tissues (Figure 4c).

Given the ability of $TEPP_{P16SP}$ to robustly activate T cells in vitro and selectively induce tumor senescence in vivo, we further assessed its therapeutic efficacy in a TNBC mouse model (Figure 4d). $TEPP_{P16SP}$ achieved a tumor growth inhibition rate of 74.52% by day 26 post-treatment, significantly surpassing the rates achieved with $TEPP_{P16INK4a}$ (47.24%) and $TEPP_{ShPD-L1}$ (33.61%) (Figure 4e). Histological analyses and terminal deoxynucleotidyl transferase dUTP nick-end labelling (TUNEL) staining further confirmed that $TEPP_{P16SP}$ markedly suppressed tumor cell proliferation and significantly induced apoptosis (Figure 4g–i).

Importantly, no significant changes in body weight were observed during the course of TEPP treatment (Figure 4f), indicating good systemic tolerance. Histological staining of major organs indicated no pathological abnormalities, and comprehensive blood biochemical and hematological analyses showed no

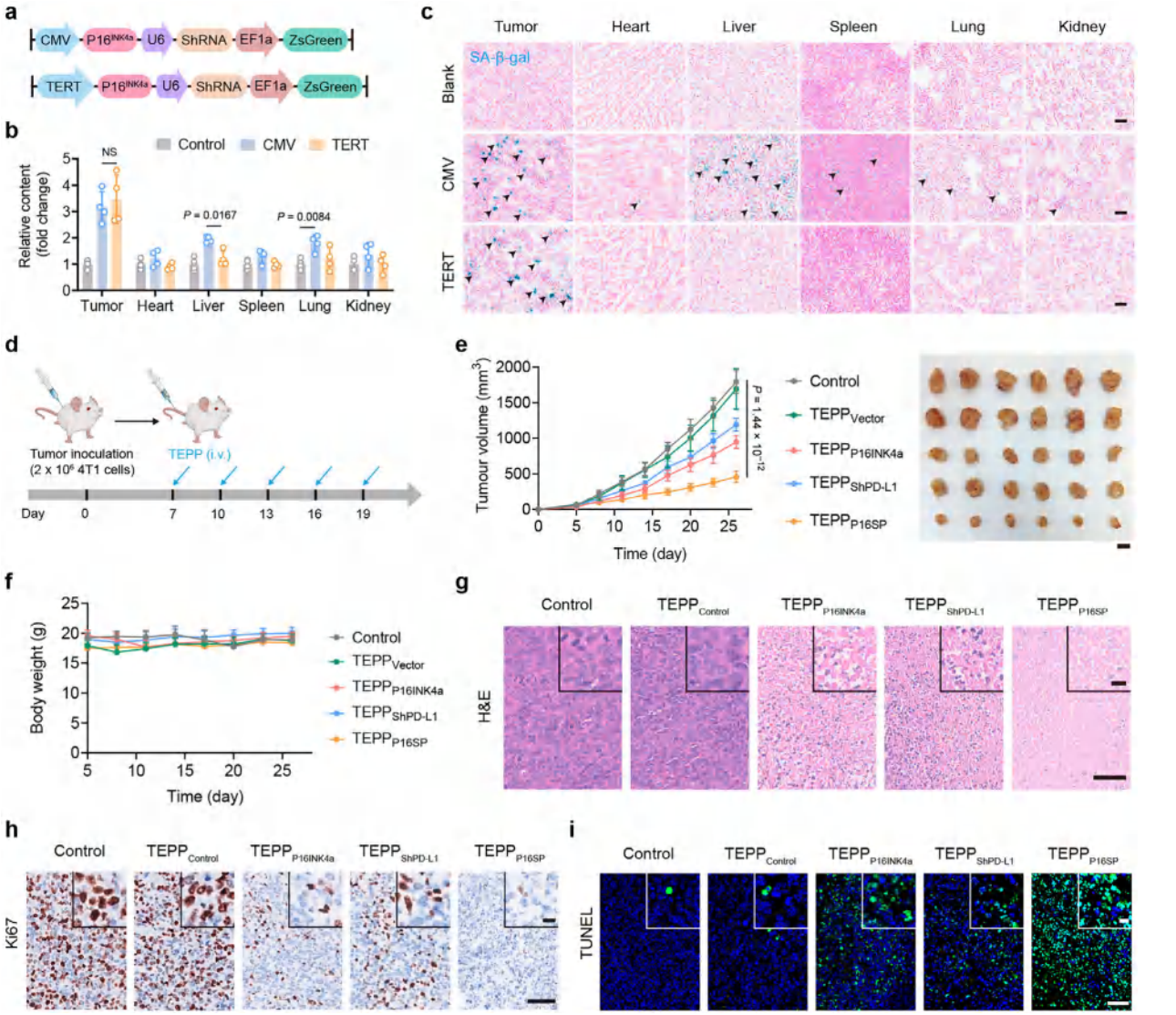

Figure 4. The TERT promoter selectively enhances $TEPP_{P16SP}$ expression and suppresses TNBC tumor progression. a) Schematic illustration of co-regulatory plasmids containing either CMV or TERT promoters for driving $P16^{INK4a}$ expression. b,c) Following intravenous administration of TEPP nanoparticles carrying plasmids with different promoters in TNBC tumor-bearing mice, $P16^{INK4a}$ protein expression in tumors and major organs was quantified by ELISA (b), and cellular senescence was visualized by SA-β-gal staining (c) (n = 4 independent samples). d) Schematic depiction of the subcutaneous TNBC mouse model and the TEPP treatment regimen. e) Tumor growth curves and representative photographs of excised tumors on day 26 after treatment (n = 6). Scale bar: 1 cm. f) Body weight monitoring of TNBC mice throughout the treatment period (n = 6). g–i) Representative images of tumor sections stained with H&E (g), Ki67 immunohistochemistry (h), and TUNEL (i) following different treatments. Scale bar: 50 μm (insets, 10 μm). Data in (b,e,f) are presented as mean ± s.d. P values calculated using two-way ANOVA with Tukey's post hoc correction (b) or one-way ANOVA with Tukey's post hoc correction (e).

detectable adverse effects (Figure S26, Supporting Information). Collectively, these results demonstrated the favorable biosafety profile of the TEPP and supported its potential for clinical translation as a systemic gene delivery system.

2.6. $TEPP_{P16SP}$ Reshapes the Immunosuppressive TME

To investigate the mechanisms underlying the antitumor effects of $TEPP_{P16SP}$, we conducted comprehensive transcriptomic analyses of TNBC tumor tissues after treatment. The results showed significant transcriptomic alterations induced by $TEPP_{P16SP}$, with 1037 genes upregulated and 342 genes downregulated compared to the control group ($P < 0.05$, fold change ≥ 2) (**Figure** 5a). Kyoto Encyclopedia of Genes and Genomes (KEGG) pathway analysis showed that $TEPP_{P16SP}$ primarily impacted pathways associated with signal transduction and immune system processes (Figure 5b). Further enrichment analysis indicated that these changes were primarily associated with T cell-mediated cytotoxicity and antigen processing and presentation (Figure 5c,g). Gene Ontology (GO) enrichment analysis corroborated these results, showing the activation of immune system pathways and

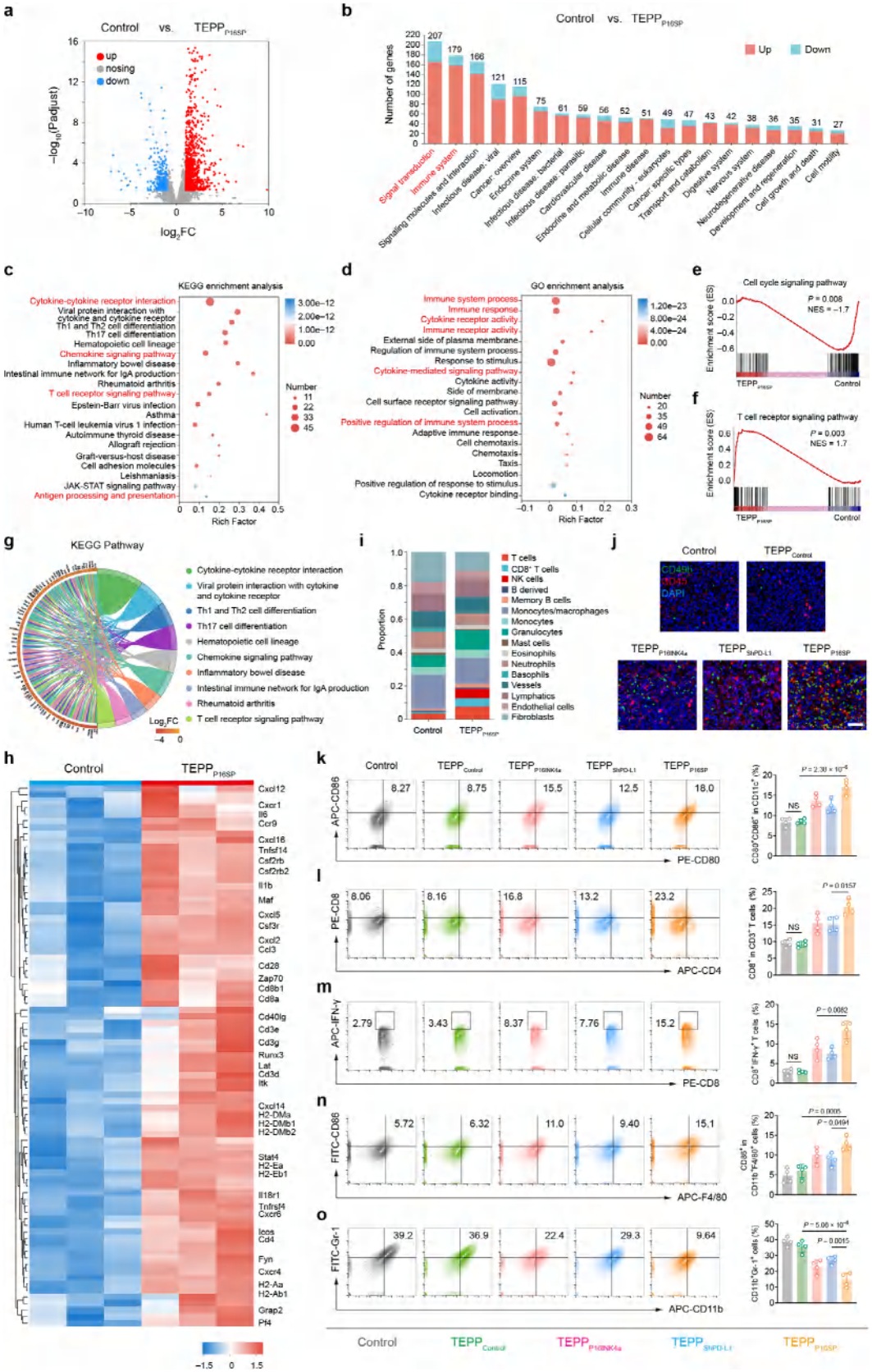

cytokine receptor activity (Figure 5d). Gene Set Enrichment Analysis (GSEA) identified the cell cycle and T cell receptor signaling as key pathways modulated by $TEPP_{P16SP}$. Notably, suppression of cell cycle-induced SASP triggered a robust immune response through enhanced T cell recruitment and activation (Figure 5e,f and Figure S27, Supporting Information). Clustering of differentially expressed genes further showed significant upregulation of genes involved in T cell recruitment and activation, such as *Cxcl12*, *Cd8a*, and *Cd28*. Furthermore, proinflammatory cytokines in the TME, including *Il6* and *Il1b*, were markedly upregulated. Significantly, genes associated with antigen presentation, including *H2-Aa*, *H2-Ab1*, and *H2-Eb1*, were elevated as well, suggesting that $TEPP_{P16SP}$ treatment enhanced tumor immunogenicity and promoted T cell-mediated tumor eradication (Figure 5h).

The Microenvironment Cell Populations-counter (MCP-counter) analysis was used to assess changes in TME-associated cell populations. This analysis revealed significant increases in NK and T cells, especially $CD8^+$ T cells, after $TEPP_{P16SP}$ treatment. This increase was accompanied by a marked decrease in fibroblasts (Figure 5i). Immunofluorescence staining further corroborated these results, showing substantially enhanced NK cell infiltration in the $TEPP_{P16SP}$-treated group compared to the other treatment groups (Figure 5j). FCM analysis of immune cells in tissue samples showed that the proportion of mature dendritic cells (DCs) in the inguinal lymph nodes was 17.1% in the $TEPP_{P16SP}$ group. This represented a 2.04- and 2.00-fold increase compared to the control and $TEPP_{Vector}$ groups, respectively (Figure 5k). Notably, the proportion of $CD8^+$ T cells, especially those secreting IFN-γ, increased 1.82- and 5.99-fold in the tumor tissue of the $TEPP_{P16SP}$-treated group compared to the control group (Figure 5l,m). Furthermore, $TEPP_{P16SP}$ treatment significantly increased the proportion of pro-inflammatory M1 macrophages while reducing immunosuppressive myeloid-derived suppressor cells (MDSCs) (Figure 5n,o). Collectively, these results indicated that $TEPP_{P16SP}$ treatment effectively remodeled the immunosuppressive TME by activating both innate immunity, including NK cells, and adaptive immunity, particularly $CD8^+$ T cells, thereby enhancing antitumor immune surveillance.

2.7. Antitumor Effects of $TEPP_{P16SP}$ Combined with ICB

Encouraged by the potent ability of $TEPP_{P16SP}$ to reshape the TME, we investigated whether $TEPP_{P16SP}$ could enhance the efficacy of ICB therapy. As shown in **Figure 6a**, CRC tumor-bearing mice were treated with $TEPP_{P16SP}$, αCTLA-4, or both in combination. The combination therapy resulted in a marked improvement in therapeutic efficacy, with a tumor inhibition rate of 91.8%, significantly surpassing that of the αCTLA-4 monotherapy group (36.5%) and the $TEPP_{P16SP}$ monotherapy group (65.2%) (Figure 6b,c). Notably, $TEPP_{P16SP}$ significantly enhanced the capacity of αCTLA-4 to deplete regulatory T cells (Tregs) in the TME. The proportion of Tregs in the combination treatment group decreased by 1.45-fold compared to the control group (Figure 6d,e). In addition, $TEPP_{P16SP}$ treatment significantly increased $P16^{INK4a}$ expression at the tumor site and robustly promoted $CD8^+$ T cell infiltration and granzyme B secretion (Figure S28, Supporting Information). These results suggested that the combination of $TEPP_{P16SP}$ and αCTLA-4 therapy effectively reversed the immunosuppressive TME and elicited a potent antitumor immune response in CRC.

To further assess the therapeutic efficacy of the combination therapy in preventing tumor metastasis, a TNBC lung metastasis model was established (Figure 6f). The control group showed rapid tumor progression and robust bioluminescent signals within 28 days. In contrast, the $TEPP_{P16SP}$+αCTLA-4 combination group exhibited minimal bioluminescence, suggesting effective suppression of metastatic spread (Figure 6g). Photographic and histological analyses of lung tissues further confirmed these results, showing extensive metastases in the control and monotherapy groups, while the combination therapy group exhibited nearly complete inhibition of lung metastases (Figure 6h). Quantitatively, the number of metastatic nodules was reduced by 10.93-fold compared to the control group (Figure 6i), and median survival was significantly extended from 29to 60 days (Figure 6j). To investigate the underlying immune mechanisms, memory T cell populations in the spleen were analyzed (Figure 6k). The combination therapy led to a 5.88-fold increase in central memory T cells (T_{CM}) and a 3.29-fold increase in effector memory T cells (T_{EM}) compared to the control group (Figure 6l,m). Furthermore, both $CD4^+$ and $CD8^+$ T cells were robustly mobilized to the metastatic sites, contributing to the effective clearance of disseminated tumor cells (Figure S29, Supporting Information). These results showed that $TEPP_{P16SP}$ significantly enhanced the efficacy of ICB in metastatic TNBC by promoting durable antitumor immunity and strengthening the immune memory.

Furthermore, an in situ TNBC postoperative recurrence model was established to evaluate the effects of the combination therapy on the tumor stroma and immune microenvironment (Figure S30a, Supporting Information). The results showed that the combination therapy markedly suppressed postoperative TNBC

Figure 5. $TEPP_{P16SP}$ treatment reshapes the tumor immune microenvironment. a) Volcano plot showing differentially expressed genes (DEGs) between control and $TEPP_{P16SP}$ groups ($p < 0.05$, fold change ≥ 2). b) KEGG pathway enrichment analysis presented as a stacked bar chart. c,d) KEGG (c) and GO (d) enrichment analyses of pathways associated with DEGs between control and $TEPP_{P16SP}$ groups. e,f) GSEA pathway analyses highlighting cell cycle signaling (e) and T cell receptor signaling (f) pathways. g) Chord diagram illustrating associations between DEGs and enriched KEGG pathways. h) Heatmap depicting expression profiles of immune-related genes in TNBC tissues following $TEPP_{P16SP}$ treatment. i) Quantitative assessment of stromal and immune cell infiltration in TNBC tissues determined using MCP-counter analysis based on transcriptomic data. j) Representative immunofluorescence staining of CD49b and CD45 in tumor tissues from different treatment groups. Scale bar: 50 µm. k–o) FCM analysis and quantification of immune cell populations in TNBC-bearing mice after the indicated treatments: mature dendritic cells ($CD80^+CD86^+$ in $CD11c^+$) in inguinal lymph nodes (k), $CD8^+$ cytotoxic T cells ($CD8^+$ in $CD3^+$) (l), IFN-γ^+ $CD8^+$ T cells ($CD8^+$IFN-γ^+ in $CD3^+$) (m), M1 macrophages ($CD86^+$ in $CD11b^+F4/80^+$) (n), and MDSCs ($CD11b^+Gr\text{-}1^+$) in tumor tissues (o). $n = 4$ independent samples. Data in (k–o) are shown as mean ± s.d. *P* values were calculated using an unpaired two-tailed Student's *t*-test (a), Fisher's exact test with Benjamini–Hochberg correction for multiple comparisons (c,d), permutation test (e,f), or one-way ANOVA with Tukey's post hoc correction (k–o).

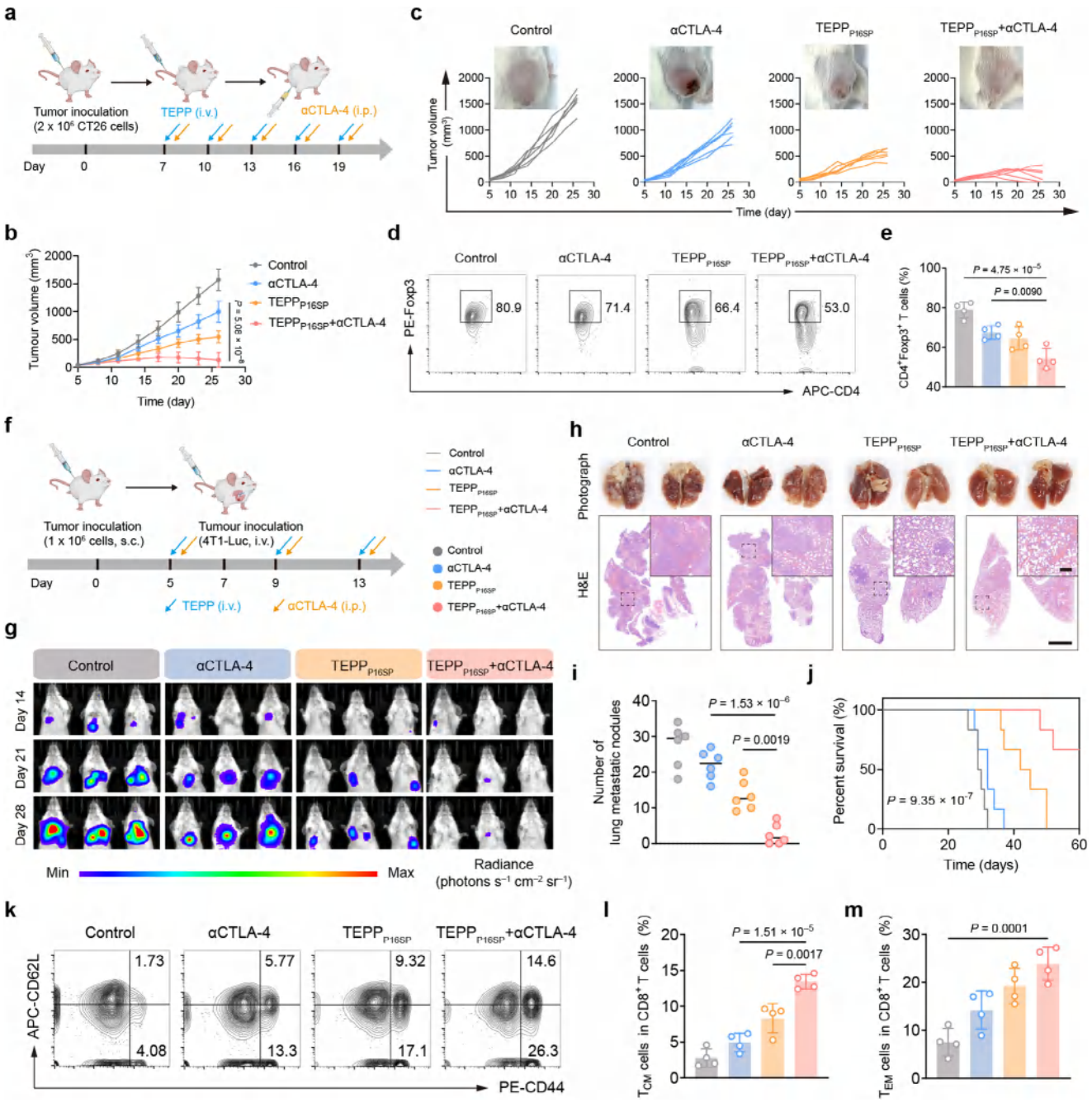

Figure 6. Antitumor efficacy of $TEPP_{P16SP}$ in combination with ICB in CRC and TNBC lung metastasis models. a) Schematic illustration of the subcutaneous CRC model and treatment schedule for $TEPP_{P16SP}$-enhanced ICB therapy. b) Tumor growth curves of CRC-bearing mice under different treatments over 26 days and c) representative tumor photographs with corresponding tumor volume quantification. n = 6 independent mice. d) Representative FCM plots and e) quantitative analysis of Tregs ($CD4^+Foxp3^+$ in $CD3^+$) in tumor tissues after treatment. n = 4 independent samples. f) Schematic representation of the TNBC lung metastasis model and treatment regimen. g) In vivo bioluminescence imaging of TNBC lung metastasis-bearing mice treated with PBS, αCTLA-4, $TEPP_{P16SP}$, or the combination therapy. Three representative mice are shown per group. h) Representative lung photographs and H&E-stained sections from each group, and i) quantification of metastatic nodule counts. Scale bar: 2 mm (inset: 250 μm). n = 6 independent mice. j) Survival curves of TNBC lung metastasis-bearing mice receiving the indicated treatments. n = 6 independent mice. k–m) Representative FCM plots (k) and quantitative analyses of T_{CM} ($CD44^+CD62L^+$ in $CD8^+$) (l) and T_{EM} ($CD44^+CD62L^-$ in $CD8^+$) (m) in spleens of TNBC lung metastasis-bearing mice after treatment. n = 4 independent samples. Data in (b,e,i,l,m) are presented as mean ± s.d. P values were calculated using one-way ANOVA with Tukey's post hoc correction (b,e,i,l,m) or log-rank (Mantel-Cox) test (j).

recurrence compared with both the control and monotherapy groups, without causing significant body weight loss (Figure S30b–d, Supporting Information). The treatment effectively inhibited the rapid proliferation of recurrent tumor lesions and promoted extensive T-cell infiltration, resulting in robust immune activation (Figure S30e, Supporting Information). FCM analysis further revealed that the levels of T_{CM} and T_{EM} in the spleens of mice receiving combination therapy were significantly increased compared with the control group, indicating durable postoperative tumor control (Figure S30f,g, Supporting Information). In addition, the Apc^{KO} mouse model was used to simulate the development of human CRC (Figure S31a, Supporting Information). Following the treatment cycle, intestinal tissues were harvested for imaging and quantitative analysis. The results showed that the combination therapy significantly reduced intestinal tumor burden, decreasing the number of spontaneous tumors by approximately 5.5-fold compared with the control group (Figure S31b,c, Supporting Information). In vivo ultrasound (US) imaging further demonstrated that the combination therapy effectively prevented and controlled intestinal tumor development, whereas pronounced tumor signals were observed in the control group (Figure S31d, Supporting Information). Collectively, these results demonstrated that the combination therapy achieved potent inhibition of both primary tumor initiation and postoperative recurrence, highlighting its strong potential for clinical translation.

3. Conclusion

We demonstrated that the targeted co-overexpression of $P16^{INK4a}$ and knockdown of PD-L1 via $TEPP_{P16SP}$ effectively reprograms the tumor senescence-immune axis. This dual modulation strategy enhanced tumor immunogenicity through SASP induction while concurrently mitigating PD-L1-mediated immune tolerance, thereby reinforcing T cell-dependent antitumor immunity. We further identified uPAR, a surface protein that was selectively upregulated during tumor senescence, as an optimal target for self-amplified nanoparticle delivery. Based on this, we developed TEPP, a targeted gene delivery nanoparticle that achieves tumor-specific enrichment through both CS-mediated tumor homing and uPAR antibody-mediated targeting. The incorporation of a TERT promoter and an NLS-MTAS peptide ensured precise nuclear localization and tumor-cell-specific expression of therapeutic genes. $TEPP_{P16SP}$ exhibited robust antitumor efficacy and induced potent immune responses in TNBC models. It also significantly enhanced tumor immune surveillance and memory immune responses, thereby improving the efficacy of ICB therapy in subcutaneous, lung metastasis, postoperative recurrence, and spontaneous tumor models.

Compared to conventional senescence-inducing agents, such as CDK4/6 inhibitors or other small molecules, our system achieves spatiotemporal control of senescence reprogramming while avoiding systemic toxicity. Unlike systemic PD-L1 inhibitors, $TEPP_{P16SP}$ selectively silences PD-L1 within the tumor microenvironment, thereby reducing the risk of off-target immune-related adverse events. Notably, the self-amplifying uPAR-targeting mechanism further enhances delivery precision, an advantage not achievable with passive nanocarriers. Our study highlights the clinical potential of inducing tumor-specific senescence reprogramming to improve targeted gene delivery and enhance immunotherapeutic outcomes in solid tumors.

Despite its efficacy, several aspects warrant further investigation. First, the reliance on uPAR for targeting may limit efficacy in tumors with low or heterogeneous uPAR expression. Future efforts should explore additional senescence-associated surface markers to broaden applicability. Second, while SASP enhances immunogenicity, prolonged cytokine secretion may inadvertently promote pro-tumorigenic effects in neighboring tissues. Strategies to temporally regulate SASP activity are needed. Third, our current evaluation is limited to CRC and TNBC models. It is essential to expand to stroma-rich tumors, such as pancreatic carcinoma, and to widespread metastasis models to assess broader translational relevance.

Looking forward, $TEPP_{P16SP}$ provides a modular platform adaptable to diverse combination regimens. Incorporation with oncolytic viruses or attenuated *Salmonella* could further enhance tumor-selective delivery, while combination with adoptive cell therapies (CAR-T, CAR-NK) may generate sustained and amplified immune responses. By synchronizing senescence induction with checkpoint blockade, this strategy offers a blueprint for overcoming resistance in immunologically "cold" tumors.

4. Experimental Section

Materials: The 1-(3-aminopropyl)-4-methylpiperazine, 1,4-bis(acryloyloxy)butane, 4-amino-1-butanol, N-(3-dimethylaminopropyl)-N′-ethylcarbodiimide hydrochloride and N-hydroxysuccinimide were procured from Aladdin Biochemical Technology. Chondroitin sulfate was obtained from Sangon Bioengineering. Doxycycline (HY-N0565A) and puromycin (HY-K1057) were purchased from MedChemExpress. The NLS-MTAS peptide was synthesized by Moonbiochem. The SA-β-gal staining kit was obtained from Solarbio Science & Technology Co., Ltd. The cell cycle analysis kit was obtained from Beyotime Biotechnology. Enzyme-linked immunosorbent assay (ELISA) kits for IL-1β, CCL5, CXCL1, CXCL9, and CXCL10 were obtained from ELK Biotechnology, while kits for IL-1α and IL-6 were procured from 4A Biotech. Roswell Park Memorial Institute (RPMI) 1640 medium, fetal bovine serum (FBS), and phosphate-buffered saline (PBS) were purchased from Gibco. The recombinant anti-uPAR antibody was obtained from Sino Biological. Recombinant mouse IL-2 was sourced from PeproTech, and recombinant mouse GM-CSF and IL-4 were acquired from Chamot Biotechnology Co., Ltd. InVivoMAb anti-mouse CTLA-4 (Clone no. 9D9) was purchased from BioXCell.

Cell Culture: The 4T1 and CT26 cell lines were obtained from the China Center for Type Culture Collection. Cells were maintained in RPMI-1640 medium containing 10% fetal bovine serum (FBS) and 100 U mL^{-1} penicillin-streptomycin. The stable 4T1-Vector and 4T1-$P16^{INK4a}$ cell lines were established via lentiviral transduction with Vector and $pP16^{INK4a}$ plasmids, respectively, followed by selection with 5 µg mL^{-1} puromycin. The 4T1-Luc cell line was constructed through stable adenoviral transfection with a luciferase-expressing plasmid and maintained under the same selective conditions. All cultures were incubated at 37 °C in a humidified incubator with 5% CO_2.

Plasmid Construction: The coding sequence (CDS) of $P16^{INK4a}$ was obtained from the NCBI database (accession number: NM_001040654.1) and provided in Table S1. The shRNA sequence used for PD-L1 knockdown was provided in Table S2. The TERT promoter sequence was modified according to previous studies.[41] To construct the pCMV-mCdkn2a-U6-Neo plasmid, a gene-synthesized *Cdkn2a* fragment was inserted between the *AgeI* and *XhoI* restriction sites of the pCMV-EGFP-U6-Neo backbone (Viraltherapy Technologies). The shRNA single-stranded DNA

oligonucleotides were synthesized, annealed into double-stranded fragments, and subsequently ligated into the linearized pCMV-mCdkn2a-U6-Neo vector using *BamHI* and *HindIII* restriction sites to generate the pP16SP plasmid.

Preparation of Nanoparticles: PP nanoparticles were prepared by combining PBAE and PBAE447-NLS-MTAS, each pre-dissolved in DMSO, at a 1:1 molar ratio. The mixture was diluted with sodium acetate buffer (25 mM, pH 5.2) to a final polymer concentration of 0.9 mg mL^{-1}. In parallel, plasmid DNA was diluted to 0.02 mg mL^{-1} using the same buffer. Equal volumes of the polymer and plasmid solutions were gently mixed by pipetting 15 times to ensure uniform complexation, followed by incubation at room temperature for 10 min to form PP nanoparticles with a polymer-to-DNA mass ratio of 45:1. Nanoparticles with other mass ratios were produced following the same procedure by adjusting the relative concentrations of the components.

For TEPP nanoparticle fabrication, an equal volume of CS-anti-uPAR solution (0.12 mg mL^{-1}), prepared in the same buffer, was added to the preformed PP dispersion. The mixture was gently pipetted 15 times and incubated at room temperature for 10 min to complete the surface modification, yielding TEPP nanoparticles. These were further purified by nanoprecipitation with two volumes of PBS, followed by centrifugal filtration. The final product was filtered through a 0.22 µm membrane and stored under appropriate conditions until use.

In Vitro Cellular Uptake and Transfection: To investigate cellular uptake of nanoparticles with varying surface modifications, formulations containing different mass ratios of CS to Ab-CS (w/w = 0, 0.25, 0.5, 1, 2, and 4) were prepared. Plasmid DNA was fluorescently labeled with YOYO-1 for visualization. 4T1-Vector and 4T1-$P16^{INK4a}$ cells (2×10^5 cells per well) were seeded in 6-well plates and cultured overnight at 37 °C in a humidified 5% CO_2 atmosphere. After treatment with the respective nanoparticle formulations for 2 h, cellular uptake was evaluated by FCM and CLSM. For macrophage uptake assessment, RAW 264.7 cells (2×10^5 cells per well) were seeded and incubated overnight under identical conditions. YOYO-1-labeled plasmid, PP, or TEPP nanoparticles were added to the cultures, and nanoparticle internalization was quantified by FCM following 2 h of incubation.

For transfection studies, 4T1 and CT26 cells (2×10^5 cells per well) were seeded in 6-well plates and allowed to adhere overnight. TEPP nanoparticles were prepared in 25 mM sodium acetate buffer (pH 5.2) as described above, then diluted in Opti-MEM to a final plasmid concentration of 2 µg mL^{-1}. When the cells reached ≈70% confluence, the culture medium was replaced with the nanoparticle-containing transfection medium. After 4 h of incubation, the medium was replaced with fresh RPMI-1640, and cells were further cultured for 40 h. Transfection efficiency was visualized by fluorescence microscopy and quantified using FCM. For cells transfected with the pcDNA3.1-CMV-Luciferase plasmid, luciferase expression was evaluated using IVIS.

Cell Cycle Analysis: To assess cell cycle distribution, 4T1 cells (2×10^5 cells per well) were seeded in 6-well plates and cultured overnight at 37 °C in a humidified 5% CO_2 incubator. The following day, cells were transfected with TEPP nanoparticles encapsulating different plasmids as described previously and incubated for 40 h. After incubation, cells were harvested by trypsinization, collected by centrifugation, and fixed in 70% cold ethanol for 2 h at 4 °C. Fixed cells were washed with PBS, resuspended in 0.5 mL of propidium iodide (PI) staining solution, and incubated for 30 min at 37 °C in the dark. Cell cycle profiles were subsequently determined by FCM.

Immune Cell-Mediated Cytotoxicity and T Cell Migration Assays: Splenocytes were isolated from BALB/c mice to assess immune-mediated cytotoxic activity. Briefly, mice were euthanized by cervical dislocation, and spleens were aseptically collected and placed on 70 µm cell strainers. The tissue was gently dissociated using the plunger of a syringe, and cells were washed with PBS containing 2% FBS to obtain a single-cell suspension. After centrifugation at 300 × *g* for 5 min at 4 °C, erythrocytes were removed using red blood cell lysis buffer. The remaining splenocytes were collected for subsequent analyses.

For the splenocyte contact-killing assay, 4T1 cells (5×10^5 cells per well) transfected with various plasmids were seeded in 6-well plates and cultured overnight at 37 °C with 5% CO_2. Splenocytes (4×10^6 cells per well) were then added and co-incubated for 12 h. After co-culture, both the supernatants and cell pellets were collected for evaluation. Cytotoxicity and immune activation were quantified using LDH release and ELISA assays.

For the T cell migration assay, transwell chambers (Corning, polycarbonate, 5.0 µm pore size) were employed. In brief, 40 h after transfection of 4T1 cells in the lower chamber with TEPP nanoparticles carrying different plasmids, 200 µL of splenocyte suspension from 4T1 tumor-bearing mice was added to the upper chamber. The system was incubated for 12 h at 37 °C in a 5% CO_2 atmosphere. Migrated cells in the lower chamber were harvested to assess T-cell migration, and the proportion of $CD8^+$ T cells was determined by FCM. Supernatants were analyzed for LDH activity and cytokine secretion via ELISA to evaluate T cell activation and cytotoxic function. In parallel experiments, 4T1 cells were pre-labeled with Calcein AM before co-culture. Following incubation with splenocytes under identical conditions, fluorescence intensity in the lower chamber was examined using CLSM and FCM to assess T cell-mediated tumor cell killing.

In Vivo Antitumor Therapy: All animal experiments were approved by the Institutional Animal Care and Use Committee of the Animal Experiment Center/A3 Laboratory, Wuhan University, and conducted in accordance with institutional guidelines for the care and use of laboratory animals (approval number WP20240068).

For the TNBC model, BALB/c mice were subcutaneously inoculated with 2×10^6 4T1 cells in the right dorsal region (day 0). When tumors reached ≈100 mm^3 (day 7), mice were randomly allocated into five groups (n = 6 per group): PBS, $TEPP_{Vector}$, $TEPP_{P16INK4a}$, $TEPP_{ShPD\text{-}L1}$, and $TEPP_{P16SP}$. Each group received intravenous injections of 100 µL of solution containing 20 µg of the corresponding plasmid every three days for a total of five treatments. Tumor length (L) and width (W) were measured at each time point, and tumor volume was calculated using the formula $V = 0.5 \times L \times W^2$. Body weight was monitored throughout the treatment period. On day 26, blood samples were collected for complete blood count and serum biochemistry analysis, and tumors and major organs were harvested for histopathological evaluation. All experiments complied with ethical standards, and tumor volume did not exceed 2000 mm^3.

For the CRC model, BALB/c mice were subcutaneously injected with 2×10^6 CT26 cells on the right flank (day 0). When tumor volume reached ≈100 mm^3 (day 7), mice were randomized into four groups (n = 6 per group): PBS, $TEPP_{P16SP}$, αCTLA-4, and $TEPP_{P16SP}$+αCTLA-4. Intravenous administration of $TEPP_{P16SP}$ (20 µg plasmid in 100 µL PBS) was performed every three days for five doses. The αCTLA-4 antibody (50 µg per mouse) was delivered intraperitoneally one day after each $TEPP_{P16SP}$ treatment. Tumor growth was monitored throughout, and tissues were collected on day 26 for histological analysis.

For the lung metastasis model, BALB/c mice were first injected subcutaneously with 1×10^6 4T1 cells (day 0). On day 7, 2×10^5 luciferase-expressing 4T1-Luc cells were administered intravenously to establish pulmonary metastases. Mice were randomly divided into four treatment groups (n = 6 per group). $TEPP_{P16SP}$ nanoparticles were injected intravenously on days 5, 9, and 13, and αCTLA-4 antibody (50 µg per mouse) was administered intraperitoneally on days 6, 10, and 14. Lung tumor progression was evaluated using an IVIS imaging system following intraperitoneal injection of D-luciferin. Survival time was recorded for each mouse. After euthanasia, the lungs were fixed in 4% paraformaldehyde, photographed, sectioned for H&E staining, and the number of metastatic nodules was quantified to assess metastatic burden.

Statistical Analysis: Sample sizes were determined based on preliminary experiments and prior literature. All experiments were performed with independent biological replicates as specified in the figure legends. Data are presented as mean ± SD. The Shapiro–Wilk test was applied to assess data normality. Statistical analyses were conducted using GraphPad Prism 9 software. Comparisons between two groups were evaluated using an unpaired two-tailed Student's t-test, while multiple group comparisons were performed using one-way ANOVA followed by Tukey's post hoc test. For analyses involving multiple parameters, two-way ANOVA with Tukey's post hoc correction was applied.

Supporting Information

Supporting Information is available from the Wiley Online Library or from the author.

Acknowledgements

K.Z. and Y.Y. contributed equally to this work. This work was supported by the National Natural Science Foundation of China (52588201, 52333004, and 22135005). All animal experiments were approved by the Institutional Animal Care and Use Committee of the Animal Experiment Center/A3 Laboratory, Wuhan University, and conducted in accordance with institutional guidelines for the care and use of laboratory animals.

Conflict of Interest

The authors declare no conflict of interest.

Data Availability Statement

The data that support the findings of this study are available from the corresponding author upon reasonable request.

Keywords

cancer treatment, cellular senescence, gene delivery, immunotherapy, PD-L1 expression

Received: August 25, 2025
Revised: November 8, 2025
Published online:

[1] S. W. Lowe, E. Cepero, G. Evan, *Nature* **2004**, *432*, 307.
[2] M. Ogrodnik, J. Carlos Acosta, P. D. Adams, F. d'Adda di Fagagna, D. J. Baker, C. L. Bishop, T. Chandra, M. Collado, J. Gil, V. Gorgoulis, F. Gruber, E. Hara, P. Jansen-Dürr, D. Jurk, S. Khosla, J. L. Kirkland, V. Krizhanovsky, T. Minamino, L. J. Niedernhofer, J. F. Passos, N. A. R. Ring, H. Redl, P. D. Robbins, F. Rodier, K. Scharffetter-Kochanek, J. M. Sedivy, E. Sikora, K. Witwer, T. von Zglinicki, M. H. Yun, et al., *Cell* **2024**, *187*, 4150.
[3] D. J. Baker, B. G. Childs, M. Durik, M. E. Wijers, C. J. Sieben, J. Zhong, R. A. Saltness, K. B. Jeganathan, G. C. Verzosa, A. Pezeshki, K. Khazaie, J. D. Miller, J. M. van Deursen, *Nature* **2016**, *530*, 184.
[4] L. Wang, L. Lankhorst, R. Bernards, *Nat. Rev. Cancer* **2022**, *22*, 340.
[5] W. Xue, L. Zender, C. Miething, R. A. Dickins, E. Hernando, V. Krizhanovsky, C. Cordon-Cardo, S. W. Lowe, *Nature* **2007**, *445*, 656.
[6] H.-A. Chen, Y.-J. Ho, R. Mezzadra, J. M. Adrover, R. Smolkin, C. Zhu, K. Woess, N. Bernstein, G. Schmitt, L. Fong, W. Luan, A. Wuest, S. Tian, X. Li, C. Broderick, R. C. Hendrickson, M. Egeblad, Z. Chen, D. Alonso-Curbelo, S. W. Lowe, *Cancer Discov.* **2023**, *13*, 432.
[7] I. Sturmlechner, C. Zhang, C. C. Sine, E.-J. van Deursen, K. B. Jeganathan, N. Hamada, J. Grasic, D. Friedman, J. T. Stutchman, I. Can, M. Hamada, D. Y. Lim, J.-H. Lee, T. Ordog, R.-M. Laberge, V. Shapiro, D. J. Baker, H. Li, J. M. van Deursen, *Science* **2021**, *374*, abb3420.
[8] I. Marin, O. Boix, A. Garcia-Garijo, I. Sirois, A. Caballe, E. Zarzuela, I. Ruano, C. S.-O. Attolini, N. Prats, J. A. López-Domínguez, M. Kovatcheva, E. Garralda, J. Muñoz, E. Caron, M. Abad, A. Gros, F. Pietrocola, M. Serrano, *Cancer Discov* **2023**, *13*, 410.
[9] L. I. Prieto, I. Sturmlechner, J. J. Goronzy, D. J. Baker, *Sci. Transl. Med.* **2023**, *15*, adg7291.
[10] H. J. Hwang, D. Kang, J. Shin, J. Jung, S. Ko, K. H. Jung, S.-S. Hong, J. E. Park, M. J. Oh, H. J. An, W.-H. Yang, Y.-G. Ko, J.-H. Cha, J.-S. Lee, *Nat. Commun.* **2025**, *16*, 353.
[11] A. Shahbandi, F.-Y. Chiu, N. A. Ungerleider, R. Kvadas, Z. Mheidly, M. J. S. Sun, D. Tian, D. A. Waizman, A. Y. Anderson, H. L. Machado, Z. F. Pursell, S. G. Rao, J. G. Jackson, *Nat. Cancer* **2022**, *3*, 1513.
[12] J. Majewska, A. Agrawal, A. Mayo, L. Roitman, R. Chatterjee, J. Sekeresova Kralova, T. Landsberger, Y. Katzenelenbogen, T. Meir-Salame, E. Hagai, I. Sopher, J.-F. Perez-Correa, W. Wagner, A. Maimon, I. Amit, U. Alon, V. Krizhanovsky, *Nat. Cell Biol.* **2024**, *26*, 1336.
[13] T.-W. Wang, Y. Johmura, N. Suzuki, S. Omori, T. Migita, K. Yamaguchi, S. Hatakeyama, S. Yamazaki, E. Shimizu, S. Imoto, Y. Furukawa, A. Yoshimura, M. Nakanishi, *Nature* **2022**, *611*, 358.
[14] M. Ruscetti, J. Leibold, M. J. Bott, M. Fennell, A. Kulick, N. R. Salgado, C.-C. Chen, Y.-j. Ho, F. J. Sanchez-Rivera, J. Feucht, T. Baslan, S. Tian, H.-A. Chen, P. B. Romesser, J. T. Poirier, C. M. Rudin, E. de Stanchina, E. Manchado, C. J. Sherr, S. W. Lowe, *Science* **2018**, *362*, 1416.
[15] M. Ruscetti, J. P. I. V. Morris, R. Mezzadra, J. Russell, J. Leibold, P. B. Romesser, J. Simon, A. Kulick, Y. Ho, M. Fennell, J. Li, R. J. Norgard, J. E. Wilkinson, D. Alonso-Curbelo, R. Sridharan, D. A. Heller, E. de Stanchina, B. Z. Stanger, C. J. Sherr, S. W. Lowe, *Cell* **2020**, *181*, 424.
[16] M. Colucci, S. Zumerle, S. Bressan, F. Gianfanti, M. Troiani, A. Valdata, M. D'Ambrosio, E. Pasquini, A. Varesi, F. Cogo, S. Mosole, C. Dongilli, M. A. Desbats, L. Contu, A. Revankdar, J. Chen, M. Kalathur, M. L. Perciato, R. Basilotta, L. Endre, S. Schauer, A. Othman, I. Guccini, M. Saponaro, L. Maraccani, N. Bancaro, P. Lai, L. Liu, N. Pernigoni, F. Mele, et al., *Cancer Cell* **2024**, *42*, 646.
[17] A. C. Y. Chen, S. Jaiswal, D. Martinez, C. Yerinde, K. Ji, V. Miranda, M. E. Fung, S. A. Weiss, M. Zschummel, K. Taguchi, C. S. Garris, T. R. Mempel, N. Hacohen, D. R. Sen, *Nat. Immunol.* **2024**, *25*, 1033.
[18] A. Chow, K. Perica, C. A. Klebanoff, J. D. Wolchok, *Nat. Rev. Clin. Oncol.* **2022**, *19*, 775.
[19] T. K. Kim, E. N. Vandsemb, R. S. Herbst, L. Chen, *Nat. Rev. Drug Discovery* **2022**, *21*, 529.
[20] F. Martins, L. Sofiya, G. P. Sykiotis, F. Lamine, M. Maillard, M. Fraga, K. Shabafrouz, C. Ribi, A. Cairoli, Y. Guex-Crosier, T. Kuntzer, O. Michielin, S. Peters, G. Coukos, F. Spertini, J. A. Thompson, M. Obeid, *Nat. Rev. Clin. Oncol.* **2019**, *16*, 563.
[21] M. D. Park, J. Le Berichel, P. Hamon, C. M. Wilk, M. Belabed, N. Yatim, A. Saffon, J. Boumelha, C. Falcomatà, A. Tepper, S. Hegde, R. Mattiuz, B. Y. Soong, N. M. LaMarche, F. Rentzeperis, L. Troncoso, L. Halasz, C. Hennequin, T. Chin, E. P. Chen, A. M. Reid, M. Su, A. R. Cahn, L. L. Koekkoek, N. Venturini, S. Wood-isenberg, D. D'souza, R. Chen, T. Dawson, K. Nie, et al., *Science* **2024**, *386*, adn0327.
[22] L. I. Prieto, I. Sturmlechner, S. I. Graves, C. Zhang, N. P. Goplen, E. S. Yi, J. Sun, H. Li, D. J. Baker, *Cancer Cell* **2023**, *41*, 1261.
[23] L. Chibaya, K. D. DeMarco, C. F. Lusi, G. I. Kane, M. L. Brassil, C. N. Parikh, K. C. Murphy, S. R. Chowdhury, J. Li, B. Ma, T. E. Naylor, J. Cerrutti, H. Mori, M. Diaz-Infante, J. Peura, J. R. Pitarresi, L. J. Zhu, K. A. Fitzgerald, P. U. Atukorale, M. Ruscetti, *Sci. Transl. Med.* **2024**, *16*, adj9366.
[24] Z. Wang, Y. Chen, H. Fang, K. Xiao, Z. Wu, X. Xie, J. Liu, F. Chen, Y. He, L. Wang, C. Yang, R. Pei, D. Shao, *Sci. Adv.* **2024**, *10*, adp7022.
[25] L. Fan, P. Du, Y. Li, X. Chen, F. Liu, Y. Liu, A. M. Petrov, X. Li, Z. Wang, Y. Zhao, *ACS Nano* **2024**, *18*, 7011.
[26] G. S. França, M. Baron, B. R. King, J. P. Bossowski, A. Bjornberg, M. Pour, A. Rao, A. S. Patel, S. Misirlioglu, D. Barkley, K. H. Tang, I. Dolgalev, D. A. Liberman, G. Avital, F. Kuperwaser, M. Chiodin, D. A. Levine, T. Papagiannakopoulos, A. Marusyk, T. Lionnet, I. Yanai, *Nature* **2024**, *631*, 876.
[27] J. Conde, R. Langer, J. Rueff, *Nat. Nanotechnol.* **2023**, *18*, 537.

[28] A. Schambach, C. J. Buchholz, R. Torres-Ruiz, K. Cichutek, M. Morgan, I. Trapani, H. Büning, *Lancet* **2024**, *403*, 568.
[29] P. Chun-on, A. M. Hinchie, H. C. Beale, A. A. Gil Silva, E. Rush, C. Sander, C. J. Connelly, B. K. N. Seynnaeve, J. M. Kirkwood, O. M. Vaske, C. W. Greider, J. K. Alder, *Science* **2022**, *378*, 664.
[30] Y. Wang, S.-K. Zhou, Y. Wang, Z.-D. Lu, Y. Zhang, C.-F. Xu, J. Wang, *Nat. Commun.* **2023**, *14*, 1993.
[31] K. Narayanan, S. K. Yen, Q. Dou, P. Padmanabhan, T. Sudhaharan, S. Ahmed, J. Y. Ying, S. T. Selvan, *Sci. Rep.* **2013**, *3*, 2184.
[32] C. Amor, J. Feucht, J. Leibold, Y.-J. Ho, C. Zhu, D. Alonso-Curbelo, J. Mansilla-Soto, J. A. Boyer, X. Li, T. Giavridis, A. Kulick, S. Houlihan, E. Peerschke, S. L. Friedman, V. Ponomarev, A. Piersigilli, M. Sadelain, S. W. Lowe, *Nature* **2020**, *583*, 127.
[33] C. Amor, I. Fernández-Maestre, S. Chowdhury, Y.-J. Ho, S. Nadella, C. Graham, S. E. Carrasco, E. Nnuji-John, J. Feucht, C. Hinterleitner, V. J. A. Barthet, J. A. Boyer, R. Mezzadra, M. G. Wereski, D. A. Tuveson, R. L. Levine, L. W. Jones, M. Sadelain, S. W. Lowe, *Nat. Aging* **2024**, *4*, 336.
[34] X. Ming, Z. Yang, Y. Huang, Z. Wang, Q. Zhang, C. Lu, Y. Sun, Y. Chen, L. Zhang, J. Wu, H. Shou, Z. Lu, B. Wang, *Nat. Aging* **2025**, *5*, 28.
[35] P. Ganguli, C. C. Basanta, A. Acha-Sagredo, H. Misetic, M. Armero, A. Mendez, A. Zahra, G. Devonshire, G. Kelly, A. Freeman, M. Green, E. Nye, A. Bichisecchi, P. Bonfanti, R. C. Fitzgerald, P. A. W. Edwards, N. Grehan, B. Nutzinger, A. M. Redmond, C. Loreno, S. Abbas, A. Freeman, E. C. Smyth, M. O'Donovan, A. Miremadi, S. Malhotra, M. Tripathi, H. Coles, C. Millington, M. Eldridge, et al., *Nat. Cancer* **2025**, *6*, 158.
[36] E. Adib, A. H. Nassar, E. W. Akl, S. Abou Alaiwi, P. V. Nuzzo, T. H. Mouhieddine, G. Sonpavde, R. I. Haddad, K. W. Mouw, M. Giannakis, F. S. Hodi, S. A. Shukla, A. Gusev, D. A. Braun, T. K. Choueiri, D. J. Kwiatkowski, *Clin. Cancer Res.* **2021**, *27*, 4025.
[37] L. Chibaya, K. D. DeMarco, C. F. Lusi, G. I. Kane, M. L. Brassil, C. N. Parikh, K. C. Murphy, S. R. Chowdhury, J. Li, B. Ma, T. E. Naylor, J. Cerrutti, H. Mori, M. Diaz-Infante, J. Peura, J. R. Pitarresi, L. J. Zhu, K. A. Fitzgerald, P. U. Atukorale, M. Ruscetti, *Sci. Transl. Med.* **2024**, *16*, adj9366.
[38] Y. Chen, Y. Huang, Q. Li, Z. Luo, Z. Zhang, H. Huang, J. Sun, L. Zhang, R. Sun, D. J. Bain, J. F. Conway, B. Lu, S. Li, *Nat. Nanotechnol.* **2023**, *18*, 193.
[39] Y. Wang, W. Deng, D. Lee, L. Yan, Y. Lu, S. Dong, K. Huntoon, A. Antony, X. Li, R. Ye, Y. Zhao, F. Zhao, B. R. Schrank, J. Ha, M. Kang, M. Yang, P. Gong, P. L. Lorenzi, L. Tan, T. D. Gallup, S. K. Tang, Z. Yang, J. Li, N. N. Sanford, H. Wang, B. Y. S. Kim, W. Jiang, *Nat. Nanotechnol.* **2024**, *19*, 255.
[40] J.-J. Lee, S. Y. Kim, S. H. Kim, S. Choi, B. Lee, J.-S. Shin, *Cell Death Dis.* **2022**, *13*, 791.
[41] X. Lin, W. Chen, F. Wei, X. Xie, *Mol. Ther.* **2021**, *29*, 244.

WILEY-VCH

Supporting Information of

Senescence Reprogramming Unleashes Tumor Immune surveillance via Coordinated Gene Modulation

*Kai Zhao†, Yu Yan†, Bao-Ting Dong, Shan-Shan Pan, Xian-Zheng Zhang**

K. Zhao, Y. Yan, B.-T. Dong, S.-S. Pan, Prof. Dr. X.-Z. Zhang
Key Laboratory of Biomedical Polymers of Ministry of Education, Department of Chemistry, Department of Traditional Chinese Medicine of Zhongnan Hospital, Wuhan University, Wuhan 430072, P. R. China

* E-mail: xz-zhang@whu.edu.cn (X.-Z. Zhang).
† These authors contributed equally to this work.

Materials and Methods.

Synthesis of PABE447-NLS-MTAS. PBAE447 was synthesized according to previous studies[2]. In brief, 1.4-bis(acryloyloxy)butane and 4-amino-1-butanol were combined at a molar ratio of 1.1:1 and reacted at 90 °C with stirring for 24 h to form acrylate-terminated poly(4-amino-1-butanol-co-1,4-butanediol diacrylate). Then, 4.6 g of the resulting polymer was dissolved in 5 ml of anhydrous tetrahydrofuran (THF), followed by the addition of 1.572 g of 1-(3-aminopropyl)-4-methylpiperazine pre-dissolved in anhydrous THF. The mixture was stirred at room temperature for 2 h to obtain the terminally capped polymer. The product was then precipitated using five volumes of cold diethyl ether, washed three times with excess diethyl ether, and dried under vacuum to obtain PBAE447.

The synthesis of PBAE447-NLS-MTAS was modified according to previous studies[3]. Specifically, 300 mg of PBAE447 was accurately weighed and dissolved in 10 ml of DMSO. Next, 24 mg of 4-(maleimido)phenyl isocyanate was added, and the mixture was stirred at room temperature for 3 h. Then, 200 mg of NLS-MTAS peptide and tri(2-carboxyethyl)phosphine (TCEP, Cat#1034385, Leyan, Shanghai, China), pre-dissolved in DMSO, were introduced and the reaction proceeded for an additional 4 h. The final product was dialyzed against deionized water for 24 h (molecular weight cutoff, 8000 Da). After freeze-drying, PBAE447-NLS-MTAS was obtained. The structures of both PBAE447 and PBAE447-NLS-MTAS were confirmed by ^{1}H NMR spectroscopy.

Synthesis of CS-anti-Upar. Chondroitin sulfate (21 mg) was dissolved in 3 ml of deionized water. To activate the carboxyl groups, 1.5 mg of N-(3-dimethylaminopropyl)-N′-ethylcarbodiimide hydrochloride and 1 mg of N-hydroxysuccinimide were added to the solution. The mixture was stirred at room temperature for 1 h. Then, 200 µl of recombinant anti-uPAR antibody was added to the reaction mixture and incubated for an additional 3 h with constant stirring. The resulting conjugate was collected and dialyzed against PBS for 48 h to remove the unreacted components. A trace amount of the final lyophilized white powder was dissolved in deuterium oxide (D_2O), and the conjugation was confirmed by ^{1}H NMR spectroscopy.

Characterization of nanoparticles. TEPP nanoparticles were prepared by loading 10 µg of plasmid DNA into a sodium acetate buffer (25 mM, pH 5.2) and diluting the mixture to a final volume of 1 ml with deionized water. Then, the particle size and zeta potential were characterized using a Zetasizer Nano ZS (Malvern Instruments). For TEM imaging, freshly prepared TEPP at a plasmid concentration of 0.8 mg ml^{-1} was deposited dropwise onto a carbon-coated copper grid. After allowing the sample to settle naturally, the grid was rinsed

three times with ultrapure water and air-dried. TEM images were acquired using a JEOL JEM-2100 microscope (200 kV).

Agarose gel electrophoresis experiments. Nanocomplexes were prepared by combining 2 μg of plasmid DNA with total PBAE at a 1:1 molar ratio in 40 μl of sodium acetate buffer (25 mM, pH 5.2). After adding 1× TAE electrophoresis buffer, the samples were subjected to agarose gel electrophoresis at 120 V for 40 min.

Encapsulation efficiency and pH-responsive release. To evaluate the plasmid loading capacity of TEPP nanoparticles, the samples were centrifuged at 14,000 rpm for 20 minutes, and the supernatant was collected. The amount of unencapsulated plasmid DNA in the supernatant was quantified using the Quant-iT PicoGreen dsDNA Reagent and Kit (ThermoFisher Scientific) according to the manufacturer's instructions. The encapsulation efficiency was calculated using the following equation: Encapsulation efficiency (%) = $(W_1-W_0)/W_1 \times 100\%$, where W_1 represents the total mass of input plasmid and W_0 represents the mass of unencapsulated plasmid in the supernatant.

To investigate the pH-responsive release behavior of TEPP, the nanoparticles were dispersed in 10 volumes of 50 mM sodium acetate buffer (pH 5.0) or PBS (pH 7.4) and incubated at 37°C. At predetermined time points (0, 6, 12, and 24 h), samples were centrifuged at 14,000 rpm for 20 minutes, and the supernatant was collected. The amount of released plasmid DNA was quantified using the Quant-iT PicoGreen dsDNA Reagent and Kit.

Cell proliferation detection. To assess cell proliferation, 4T1 and CT26 cells (2×10^5 cells per well) were seeded in 6-well plates and incubated overnight at 37 °C in a humidified atmosphere with 5% CO_2. For the colony formation assay, the 4T1 cells were transfected with TEPP nanoparticles that encapsulated various plasmids, as previously described. After 40 h of incubation, the cells were trypsinized into single-cell suspensions and reseeded into 6-well plates at a density of 500 cells per well. The cells were cultured for 14 days, fixed with 4% paraformaldehyde, and stained with 0.1% crystal violet for 30 min. The plates were then washed three times with PBS, and images were captured to evaluate colony formation. For the CCK-8 assay, the 4T1 cells were similarly transfected with TEPP nanoparticles for 40 h, then digested and seeded into 96-well plates at a density of 1,000 cells per well. After 48 h of incubation, 10 μl of CCK-8 solution was added to each well and incubated for 4 h at 37 °C with 5% CO_2. Absorbance at 450 nm was measured using a microplate reader to quantify cell viability.

In vitro activation of BMDCs. Bone marrow cells were isolated from 8-week-old C57BL/6 mice. Briefly, mice were euthanized by cervical dislocation, and the femurs and tibias were

aseptically harvested. The bone marrow was flushed out by repeatedly injecting sterile medium through the marrow cavity using a syringe. The collected bone marrow cells were cultured in RPMI-1640 medium supplemented with 10% FBS, 100 U ml^{-1} penicillin-streptomycin, 20 ng ml^{-1} recombinant mouse GM-CSF, and 10 ng ml^{-1} recombinant mouse IL-4. The cells were incubated for 7 days to induce differentiation into BMDCs, with half of the culture medium replaced every 3 days. To evaluate BMDC activation in vitro after different treatments, 4T1 cells that had been transfected with TEPP nanoparticles encapsulating various plasmids were co-cultured with BMDCs at a ratio of 1:2 for 12 h. BMDC maturation was subsequently assessed using flow cytometry (FCM).

OT-1 $CD8^+$ T cell activation and cytotoxicity assay. Female OT-1 mice (6–8 weeks old) were euthanized, and spleens were aseptically harvested. Splenic $CD8^+$ T cells were isolated using a mouse $CD8^+$ naive T cell isolation kit (Biolegend). After prestimulation, the isolated cells were cultured in Cell Feeder permeable flasks (Shanghai Hycells Biotechnology Co., Ltd.) in culture medium supplemented with recombinant mouse IL-2 (50 IU ml^{-1}). $CD8^+$ T cells were maintained ex vivo for no longer than one week. Activated OT-1 $CD8^+$ T cells were cryopreserved in Kryogene cell therapeutic cryopreservation solution (Milecell Biological Science & Technology Co., Ltd.).

For the cytotoxicity assay, B16-OVA cells (5×10^5 cells per well) previously transfected with TEPP nanoparticles encapsulating different plasmids were seeded in 6-well plates and incubated overnight at 37 °C in a humidified atmosphere containing 5% CO_2. Subsequently, OT-1 $CD8^+$ T cells were added at an effector-to-target (E:T) ratio of 1:1 and co-cultured for 12 h. After incubation, cell-mediated cytotoxicity was evaluated microscopically, and both cell pellets and culture supernatants were collected for further analysis. Cytotoxicity was quantified using an LDH release assay.

Western blot assay. After the indicated treatments, the cells were harvested and lysed using a protein extraction reagent to isolate the total cellular proteins. The protein concentrations were quantified using a bicinchoninic acid (BCA) assay kit, according to the manufacturer's instructions. Equal amounts of the protein samples were then subjected to SDS-PAGE and transferred to polyvinylidene difluoride (PVDF) membranes for Western blot analysis, which was performed according to standard protocols. The following primary antibodies were used for immunodetection: Anti-Rb (Servicebio, #GB112449, 1: 1000 dilution), Anti-PD-L1 (CST, #60475, 1: 1000 dilution), and Anti-β-Actin (Tdybio, #TDY051, 1:10000 dilution).

Immunofluorescence staining. For cell samples, the cells were cultured on slides (SAINING

Biotechnology), fixed with 4% paraformaldehyde for 15 min at room temperature, and rinsed three times with PBS. Then, the cells were permeabilized with 0.1% Triton X-100 for 15 min, washed three times with TBST, and incubated with 10% sheep serum at 37 °C for 30 min to block nonspecific binding sites. The cells were then incubated with primary antibody solution overnight at 4 °C. After washing three times with TBST, the cells were incubated with the appropriate secondary antibody at room temperature for 10 min. Nuclear staining was performed using DAPI for 5 min in the dark, followed by a final TBST wash. The samples were then observed and imaged using CLSM. For tissue samples, paraffin-embedded sections were first dewaxed using graded ethanol solutions. Then, antigen retrieval was then performed in EDTA buffer (pH 9.0) using an autoclave. Endogenous peroxidase activity was blocked with 3% hydrogen peroxide for 30 min at room temperature, followed by immersion in distilled water for 3 min. The subsequent immunofluorescence staining steps, including blocking, antibody incubation, DAPI staining, and CLSM imaging, were conducted as described for cell samples.

Fluorescence in situ hybridization (FISH) experiment. For cell samples, the cells were cultured on slides, fixed with in situ hybridization fixative for 20 minutes at room temperature, and then washed three times with PBS. The slides were then incubated with prehybridization solution at 37 °C for 1 h. Hybridization was performed overnight at 37 °C using hybridization solution containing the specific probe. The slides were then washed with saline-sodium citrate (SSC) buffer to remove the unbound probe. To block nonspecific binding sites, the cells were incubated with normal rabbit serum at room temperature for 30 min. Horseradish peroxidase-conjugated mouse anti-digoxigenin antibody (anti-DIG-HRP) was then applied, and the slides were incubated at 37 °C for 50 min. After three PBS washes, the tyramide signal amplification (TSA) reagent was added, and the samples were incubated in the dark at room temperature for 10 min. After a final wash with TBST, the slides were imaged using CLSM.

For tissue samples, the target tissue was fixed in an in situ hybridization fixative for 12 h, dehydrated through a graded ethanol series, and embedded in paraffin. The paraffin-embedded sections were then dewaxed using a graded ethanol series and rehydrated in distilled water. Antigen retrieval was performed in EDTA buffer (pH 9.0) using an autoclave. Endogenous peroxidase activity was quenched by incubating the slides in a 3% methanol–hydrogen peroxide solution in the dark at room temperature for 15 min. The subsequent FISH staining steps, including prehybridization, probe hybridization, blocking, antibody incubation, TSA signal amplification, and imaging, were carried out as described for cell samples. Sections were

visualized and recorded using CLSM.

In vivo tumor targeting and promoter-specific activation. The tumor-targeting efficacy of the nanoparticle was evaluated using a subcutaneous TNBC mouse model. Briefly, 2×10^6 4T1 cells were injected subcutaneously into the right dorsal region of BALB/c mice. Once the tumors reached a volume of approximately 100 mm^3, TOTO-3-labeled plasmids, PP, or TEPP nanoparticles were administered via intravenous injection (20 μg plasmid per mouse). The mice were sacrificed at 12 and 24 h post-injection, and the tumor tissues and major organs were harvested for imaging using IVIS to evaluate tumor accumulation and biodistribution.

To investigate promoter-specific activation, TNBC tumor-bearing mice received intravenous injections of TEPP nanoparticles loaded with plasmids driven by either the CMV- or TERT-driven plasmids (20 μg plasmid per mouse). Two days after injection, the mice were euthanized, and tumor tissues and major organs were collected for downstream analyses, including ELISA, qRT-PCR and SA-β-gal staining, to evaluate promoter-specific gene activation.

Construction and in vivo induction of the Tet-on system. The pLVX-Tet-On-Tight-mCdkn2a-PGK-Puro plasmid (Viraltherapy Technologies) was stably transduced into 4T1 and CT26 cells via lentiviral infection. A total of 2×10^6 transduced cells were subcutaneously injected into the right dorsal region of BALB/c mice to establish TNBC and CRC models, respectively. Once tumor volumes reached approximately 100 mm^3, Doxycycline was administered intraperitoneally at a dose of 5 mg kg^{-1} daily for a minimum of three consecutive days to induce tumor-specific expression of $P16^{INK4a}$. Mice in the control group received intraperitoneal injections of an equivalent volume of PBS, serving as the non-induced ($P16^{INK4a}$-off) control.

Orthotopic tumor models and treatment. For the *Apc*^{KO} mouse model, 10-week-old mice were randomly divided into four groups (n = 6 per group) and received different treatments (1 mg kg^{-1} of plasmid). Following each $TEPP_{P16SP}$ treatment, αCTLA-4 antibody (50 μg per mouse) was administered intraperitoneally on the subsequent day. This treatment cycle was repeated every 7 days for a total of three doses. Tumor growth was monitored in situ using ultrasound imaging. Mice were euthanized on day 25, and the number of intestinal tumors was quantified.

To establish the TNBC recurrence model, 2×10^6 4T1-Luc cells were implanted into the right mammary pad of female BALB/c mice on day 0. On day 7, the majority of the tumor tissue was surgically excised. The mice were then randomly divided into four groups (n = 6 per group) and administered 1 mg kg^{-1} of plasmid. Following each $TEPP_{P16SP}$ treatment, αCTLA-

4 antibody (50 μg per mouse) was administered intraperitoneally on the next day. Postoperative tumor recurrence was monitored using IVIS after the intraperitoneal injection of D-luciferin.

Transcriptomic studies. To evaluate transcriptomic alterations, 2×10^6 4T1 cells were injected subcutaneously into the right dorsal region of BALB/c mice on day 0. When tumors reached approximately 100 mm^3 on day 7, the mice were randomly divided into two groups (n = 3 per group). Each group received two intravenous administrations of either 100 μl PBS or $TEPP_{P16SP}$ (20 μg plasmid DNA per mouse). Two days after treatment, tumor tissues were harvested, rapidly frozen in liquid nitrogen, and stored at −80 °C. High-throughput RNA sequencing was performed by Majorbio BioTech Co., Ltd. The transcriptomic data were analyzed using the ISanger cloud platform (https://cloud.majorbio.com).

FCM assay. In the TNBC model with the Tet-on system, tumor tissues were harvested on days 0, 7, and 14 after induction. For the subcutaneous TNBC and CRC models, the mice were euthanized on day 26, and fresh tumor tissues along with inguinal lymph nodes were collected. In the TNBC lung metastasis model, spleens were harvested on day 28.

Tumor tissues were enzymatically digested using collagenase type IV (1 mg ml^{-1}), hyaluronidase (1 mg ml^{-1}), and DNase I (10 μg ml^{-1}) to obtain single-cell suspensions. The inguinal lymph nodes and spleens were mechanically dissociated in PBS containing 2% FBS. The resulting single-cell suspensions were stained with fluorophore-conjugated antibodies that target various immune cell populations. The following markers were used for cell subset identification: dendritic cells (fluorescein isothiocyanate (FITC) anti-mouse CD11c antibody, phycoerythrin (PE) anti-mouse CD80 antibody, allophycocyanin (APC) anti-mouse CD86 antibody), T cells (FITC anti-mouse CD3 antibody, APC anti-mouse CD4 antibody, PE anti-mouse CD8a antibody), IFN-γ^+ T cells (FITC anti-mouse CD3 antibody, APC anti-mouse IFN-γ antibody, PE anti-mouse CD8a antibody), exhausted T cells (FITC anti-mouse CD8 antibody, APC anti-mouse PD-1 antibody, PE anti-mouse TIM-3 antibody), M1 macrophages (PE anti-mouse CD11b antibody, APC anti-mouse F4/80 antibody, FITC anti-mouse CD86 antibody), MDSCs (APC anti-mouse CD11b antibody, PE anti-mouse CD45 antibody, FITC anti-mouse Gr-1 antibody) , T_{reg} cells (FITC anti-mouse CD3 antibody, APC anti-mouse CD4 antibody, PE anti-mouse Foxp3 antibody) and memory T cells (FITC anti-mouse CD8a antibody, APC anti-mouse CD62L antibody, PE anti-mouse CD44 antibody). All antibodies were sourced from Biolegend. FCM was performed using BD Accuri C6, and the data were analyzed using FlowJo software.

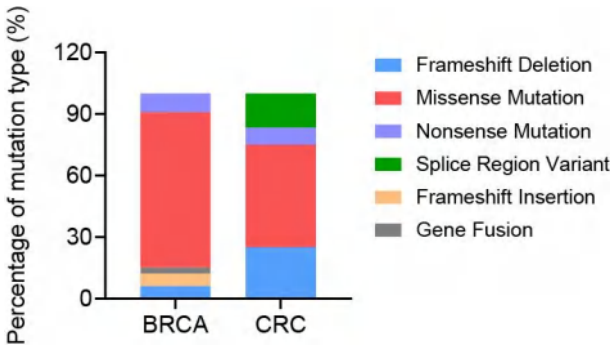

Figure S1. Specific types of *CDKN2A* mutations analyzed in BRCA and CRC.

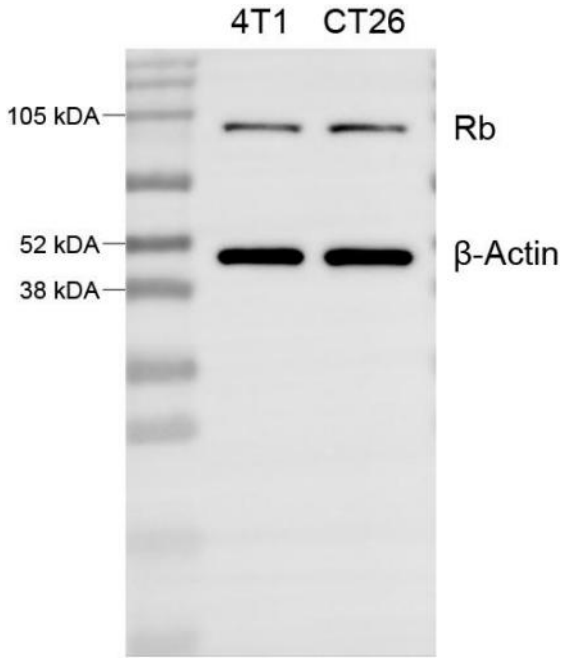

Figure S2. Western blot analysis of Rb protein expression in the 4T1 and CT26 cell lines.

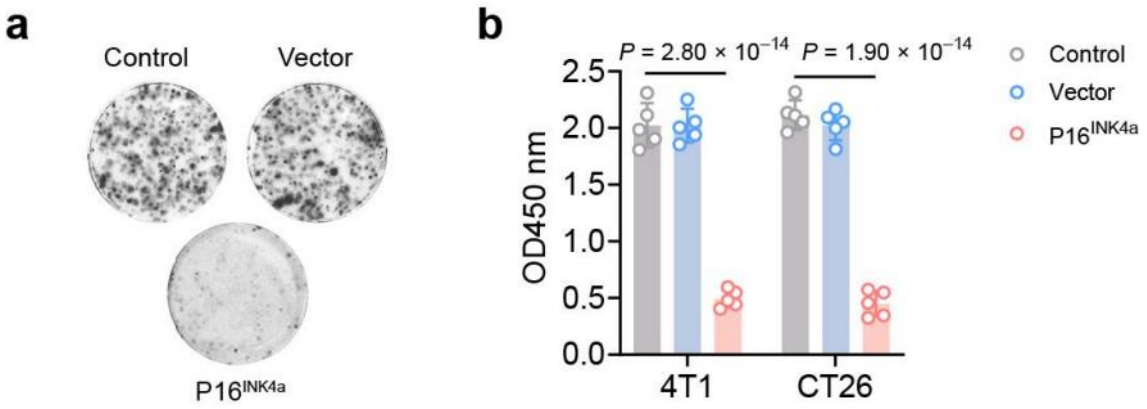

Figure S3. (a) Crystal violet staining of 4T1 cells that were either untransfected or transfected with the control vector or the pP16^{INK4a} plasmid. (b) Cell viability of 4T1 and CT26 cells that were either untransfected or transfected with the control vector or the pP16^{INK4a} plasmid, as assessed by optical density at 450 nm using the Cell Counting Kit-8 (CCK-8). $n = 5$ independent replicates. Data in (b) are presented as mean ± s.d. *P* values were determined by two-way ANOVA with Tukey's post hoc corrections (b).

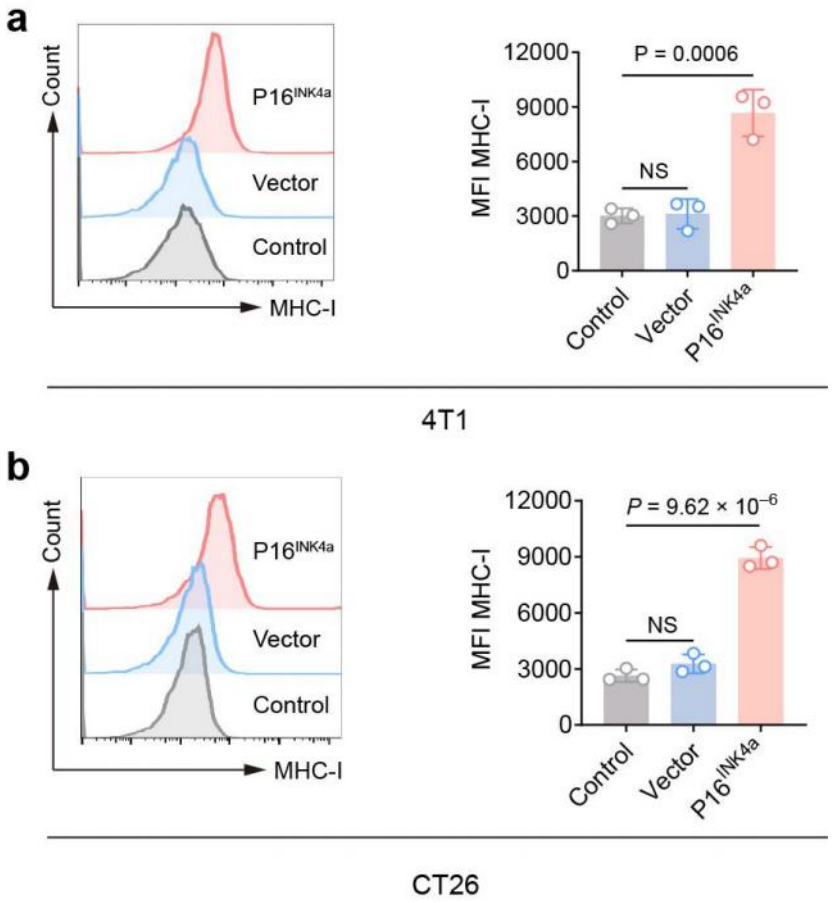

Figure S4. Representative FCM images and corresponding quantitative analysis of MFI for cell surface MHC class I molecules in (a) 4T1 cells and (b) CT26 cells that were either untransfected or transfected with the control vector or the pP16^{INK4a} plasmid. $n = 3$ independent samples. Data in (a, b) are presented as mean ± s.d. *P* values were determined by one-way ANOVA with Tukey's post hoc corrections (a, b).

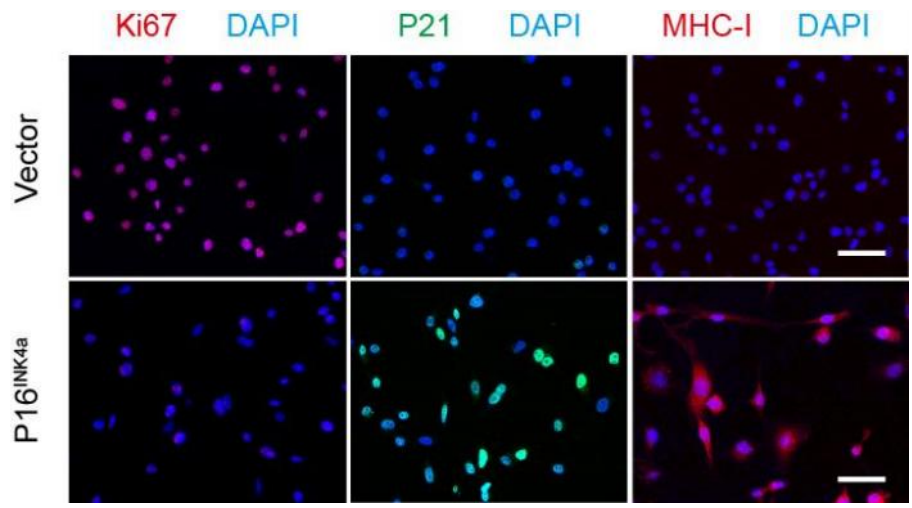

Figure S5. Representative immunofluorescence staining of Ki67, p21, and MHC class I molecules in CT26 cells that were transfected with either the control vector or the pP16^{INK4a} plasmid. Scale bar, 50 μm.

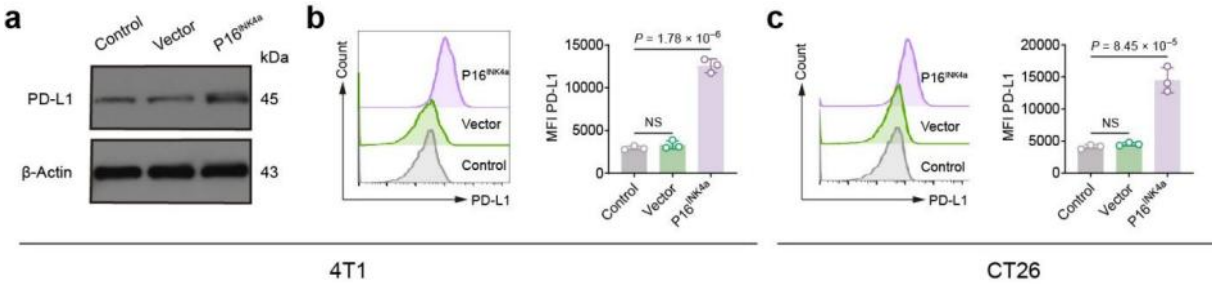

Figure S6. (a) Western blot and (b) FCM analyses of PD-L1 protein expression in 4T1, 4T1-Vector, and 4T1-P16^{INK4a} cells. $n = 3$ independent samples. (c) Representative FCM images and corresponding MFI analysis of surface PD-L1 expression in CT26, CT26-Vector, and CT26-P16^{INK4a} cells. $n = 3$ independent samples. Data in (b, c) are presented as mean ± s.d. *P* values were determined by one-way ANOVA with Tukey's post hoc corrections (b, c).

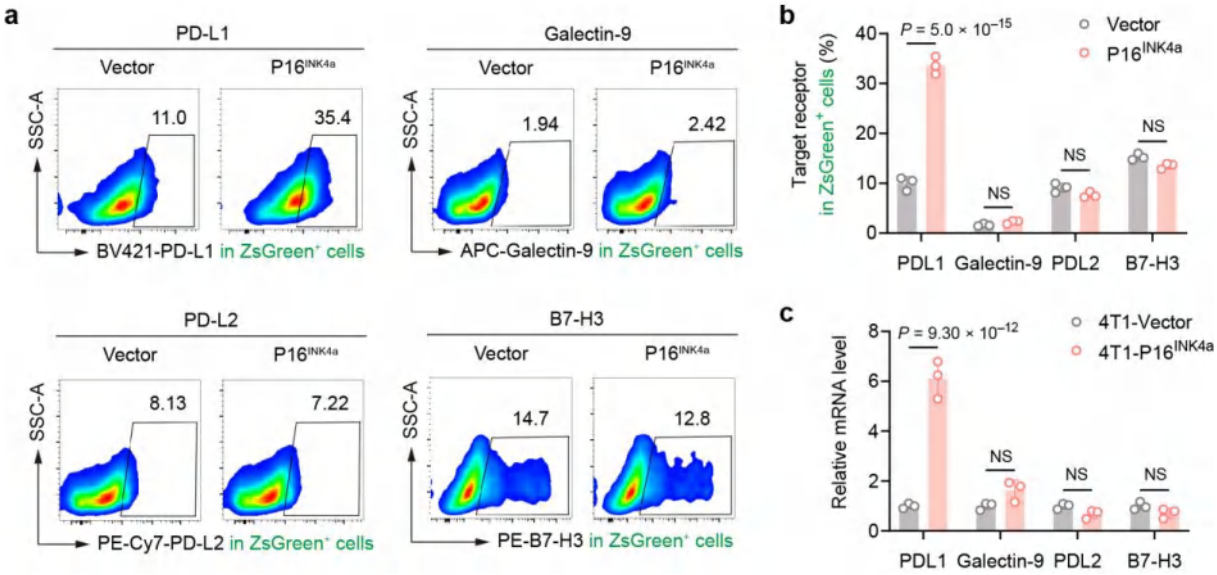

Figure S7. (a) Representative FCM images and (b) corresponding quantified analysis of surface PD-L1, Galectin-9, PD-L2, and B7-H3 expression in 4T1 cells transfected with either Vector or P16^{INK4a} plasmid, pre-gated on ZsGreen^{+} cells. n = 3 independent samples. (c) qRT-PCR analysis of PD-L1, Galectin-9, PD-L2, and B7-H3 mRNA levels in 4T1-Vector and 4T1-P16^{INK4a} cells. Data in (b, c) are presented as mean ± s.d. P values were determined by two-way ANOVA with Bonferroni's post hoc corrections (b, c).

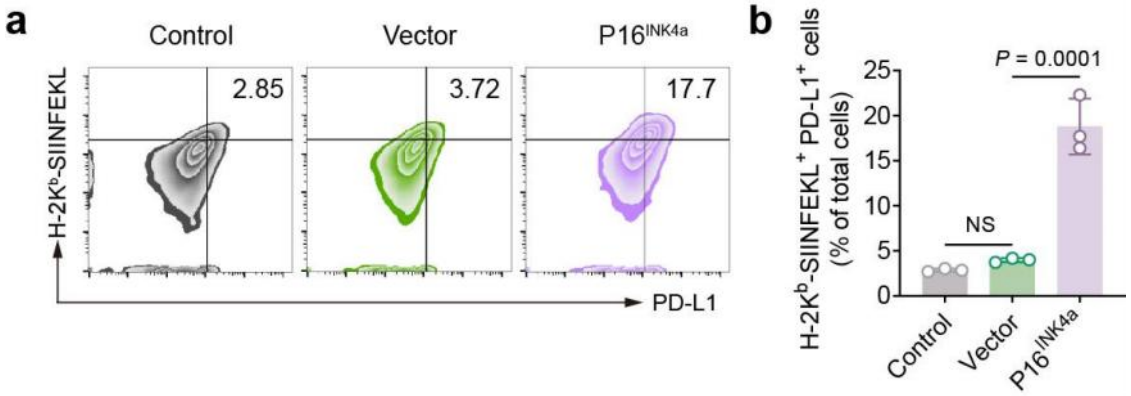

Figure S8. (a) Representative FCM images and (b) corresponding quantitative analysis of cell surface H-2K^b-SIINFEKL and PD-L1 expression in B16-OVA cells that were either untransfected or transfected with the control vector or the pP16^{INK4a} plasmid. $n = 3$ independent samples. Data in (b**)** are presented as mean ± s.d. *P* values were determined by one-way ANOVA with Tukey's post hoc corrections (b).

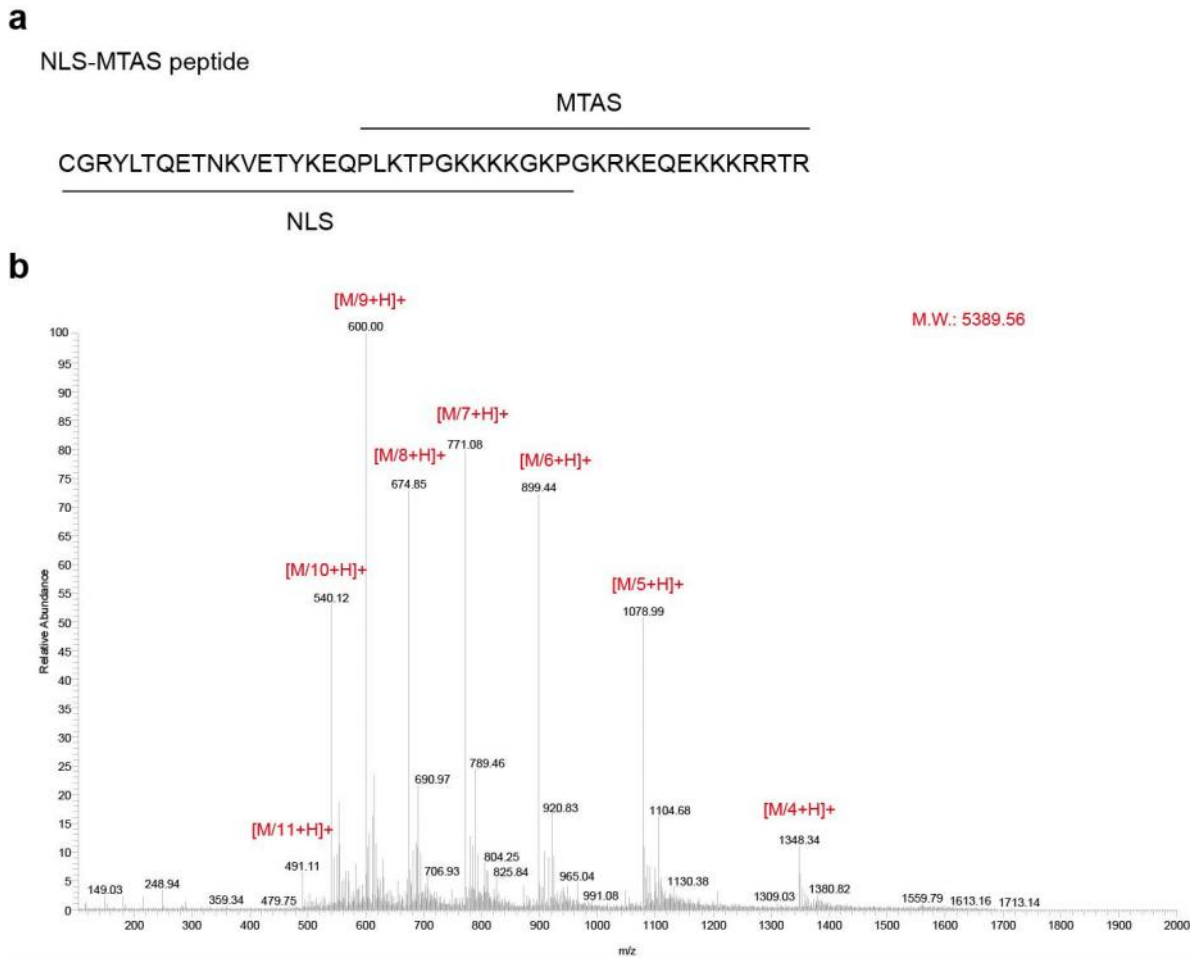

Figure S9. (a) Amino acid sequence and (b) ESI-MS analysis of the NLS-MTAS peptide.

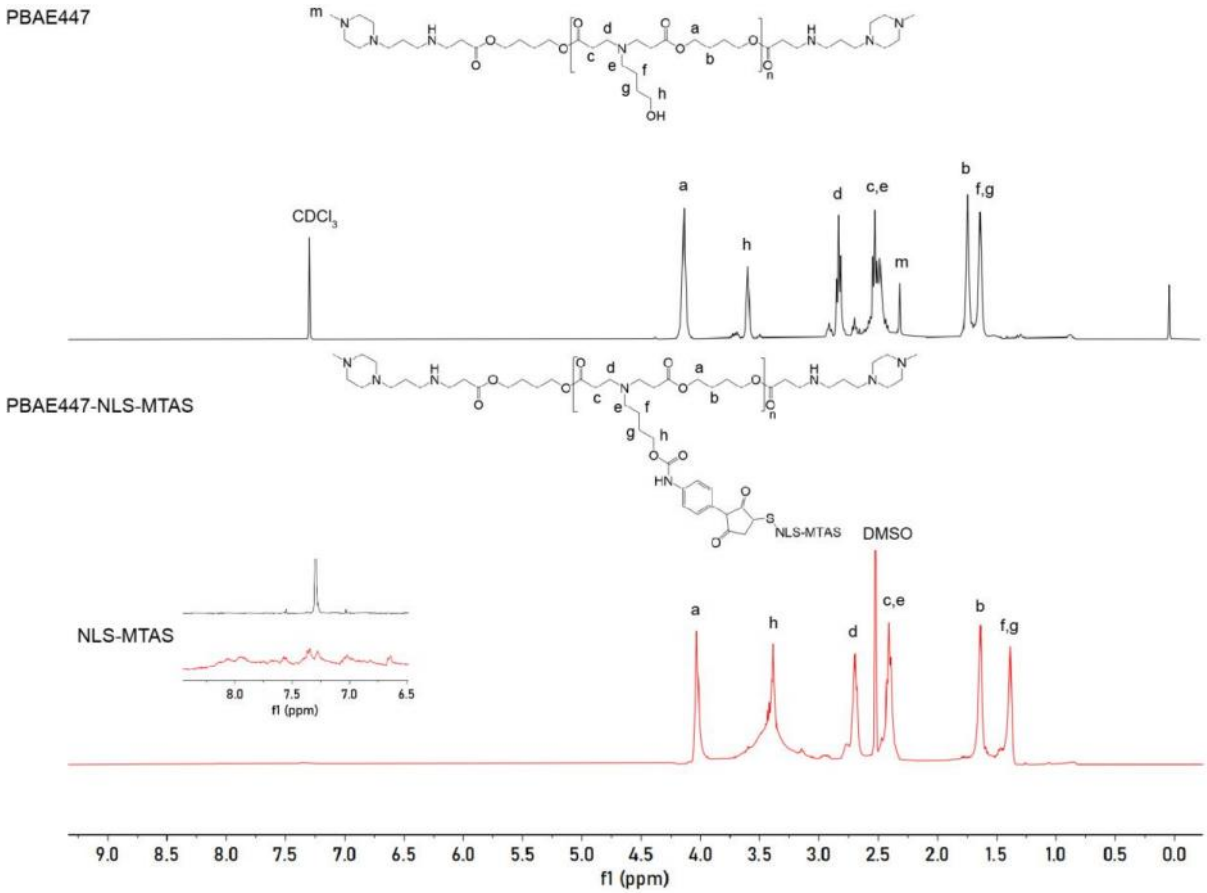

Figure S10. ^{1}H-NMR spectra of PBAE447 ($CDCl_3$) and PBAE447-NLS-MTAS (DMSO-d_6).

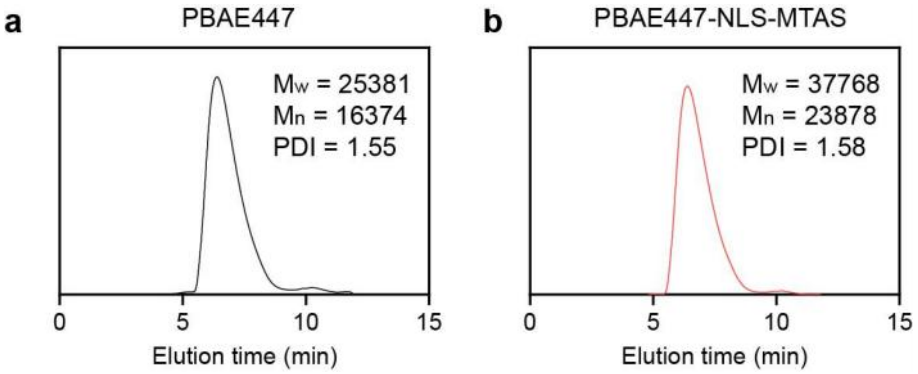

Figure S11. GPC profiles of (a) PBAE447 and (b) PBAE447-NLS-MTAS.

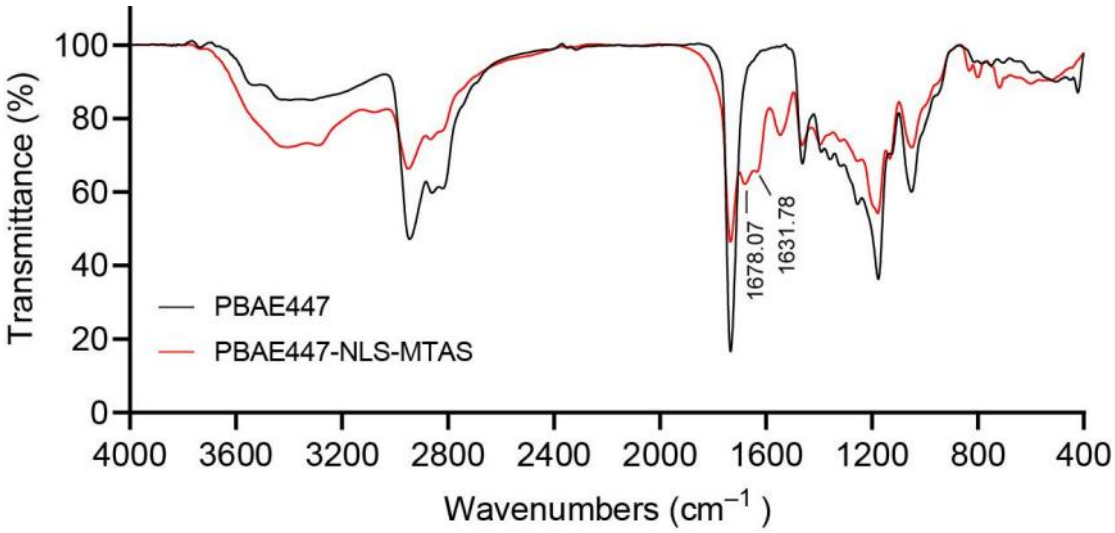

Figure S12. FTIR spectra of PBAE447 and PBAE447-NLS-MTAS.

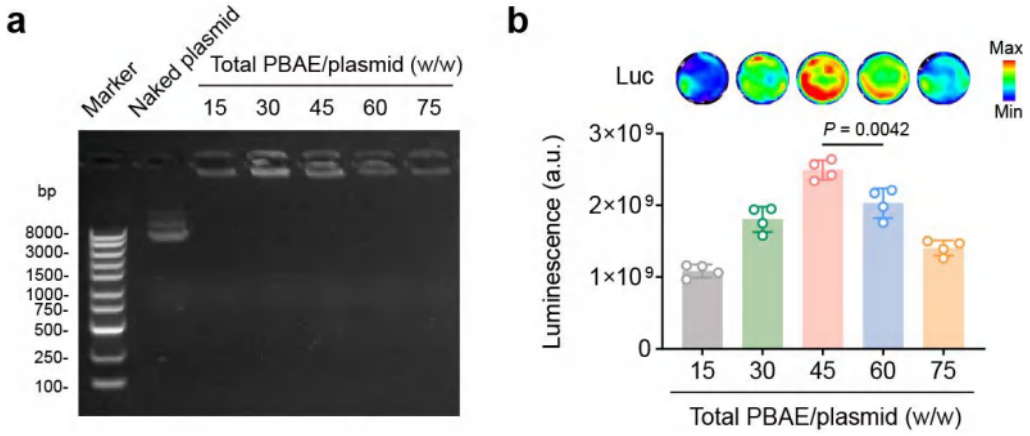

Figure S13. (a) Agarose gel electrophoresis and (b) transfection efficiency of PBAE/plasmid complexes at different mass ratios in 4T1 cells. Transfection efficiency was assessed 48 h post-transfection using the pcDNA3.1-CMV-Luciferase plasmid. $n = 4$ independent samples. Data in (b) are presented as mean ± s.d. *P* values were determined by one-way ANOVA with Tukey's post hoc corrections (b).

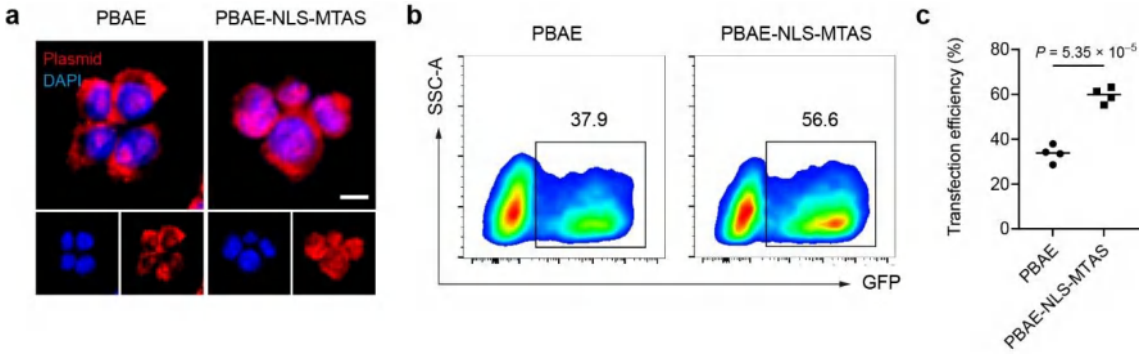

Figure S14. (a) Representative CLSM images of 4T1 cells incubated for 6 h with PBAE or PBAE-NLS-MTAS complexes containing YOYO-3-labeled plasmids, and (b) representative FCM plots with (c) corresponding quantitative analysis of transfection efficiency at 48 h. $n = 4$ independent samples. *P* values were determined by unpaired two-tailed Student's t-test (c).

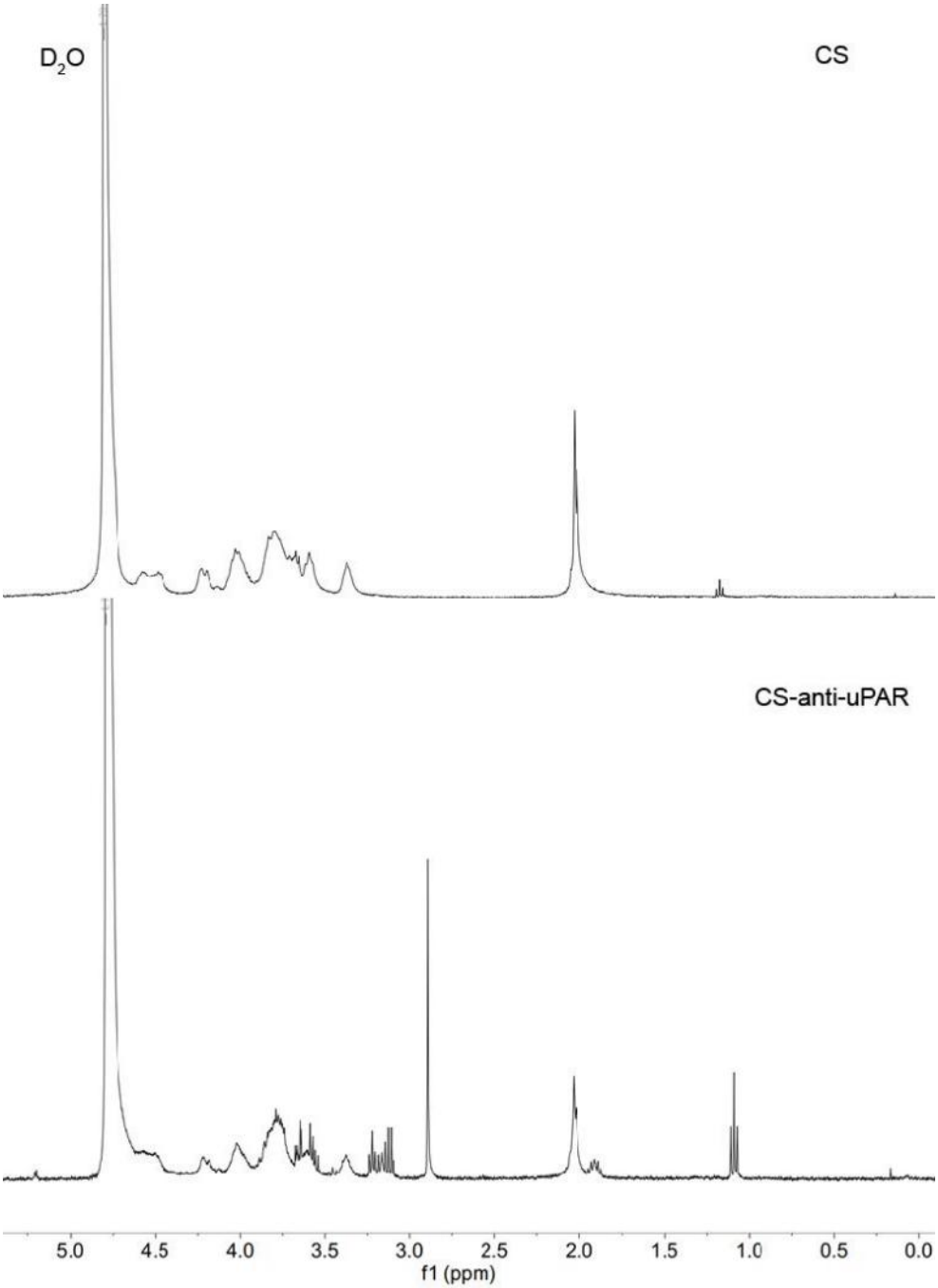

Figure S15. ^{1}H-NMR spectra of CS (D_2O) and CS-anti-uPAR (D_2O).

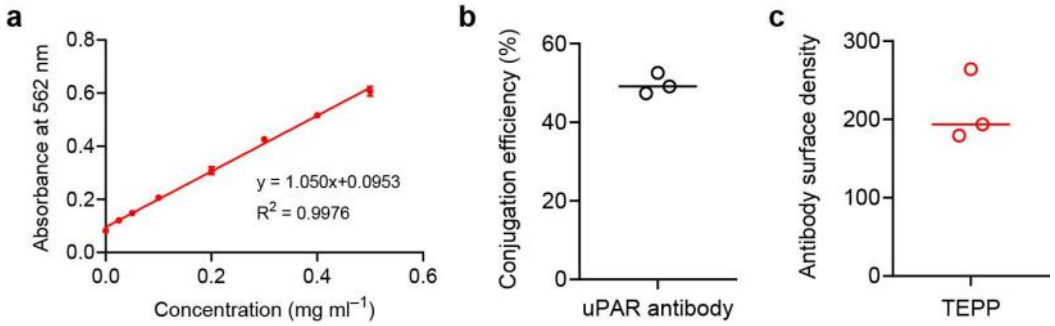

Figure S16. (a) BCA Protein Assay standard curve, (b) calculated antibody conjugation efficiency, and (c) antibody surface density per particle. n = 3 independent samples. The antibody surface density was calculated using the following equation:

Antibody surface density = [Concentration(Ab) / Mw(Ab)] × Na ÷ Concentration(NP)

where Concentration(Ab) denotes the concentration of uPAR antibody conjugated to TEPP, Mw(Ab) is approximately 150 kDa, Na represents Avogadro's constant (≈ 6.022×10^{23}), and Concentration(NP) is 2.7×10^{10} particles ml^{-1} as determined by NTA analysis.

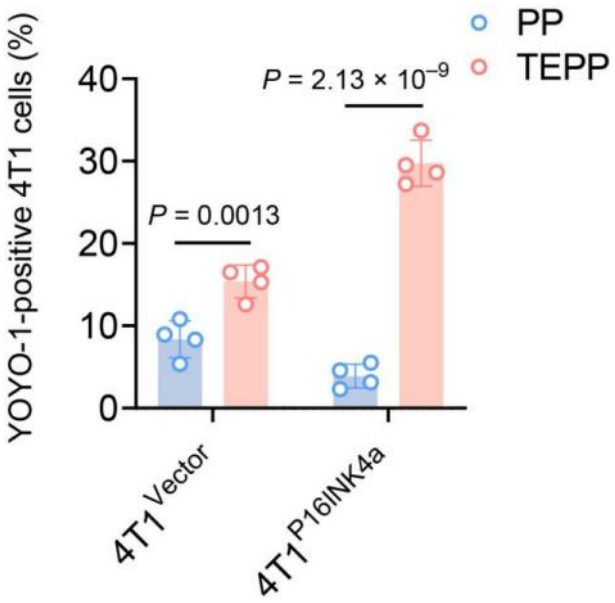

Figure S17. Quantitative statistical analysis of the internalization of YOYO-1-labeled PP and TEPP nanoparticles by 4T1-Vector and 4T1-P16^{INK4a} cells using FCM. n = 4 independent samples. Data are presented as mean ± s.d. P values were determined by two-way ANOVA with Bonferroni's post hoc corrections.

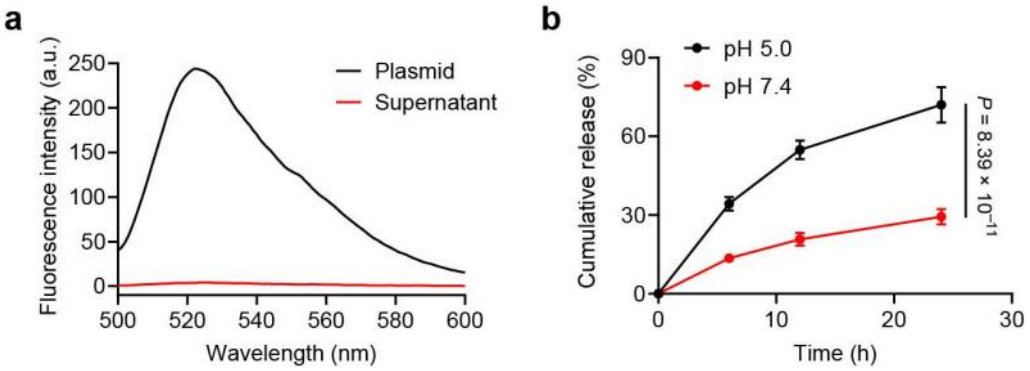

Figure S18. (a) Quantitative analysis of TEPP encapsulation efficiency and (b) pDNA release behavior under different pH conditions was performed by measuring the fluorescence intensity of plasmid DNA in the supernatant using the PicoGreen assay. n = 3 independent samples. P values were determined by two-way ANOVA with Bonferroni's post hoc corrections (b).

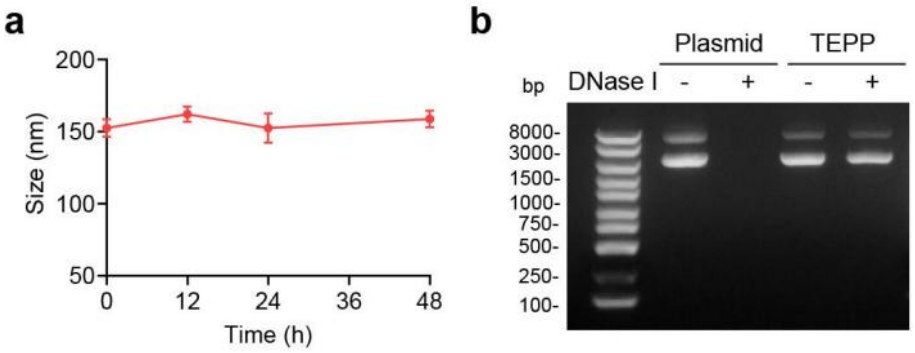

Figure S19. (a) Stability of TEPP particles in serum-containing culture medium over 48 h. n = 3 independent samples. (b) Agarose gel electrophoresis analysis of plasmid DNA and TEPP after incubation with DNase I for 30 min, followed by heparin (5 mg ml^{-1}) treatment for 2 h.

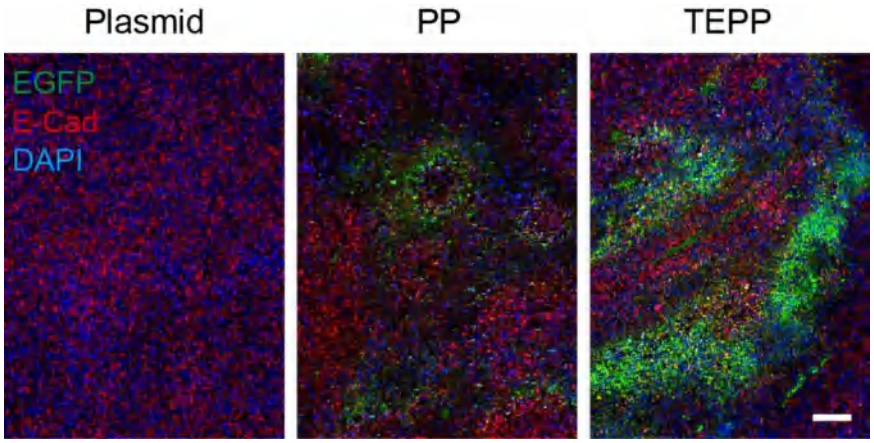

Figure S20. Representative immunofluorescence images of tumor tissues from TNBC mice captured two days after the systemic administration of the plasmid, PP and TEPP nanoparticles. Cell nucleus, DAPI. E-Cad, TNBC marker. EGFP, spontaneous expression of the plasmid. Scale bar, 100 μm.

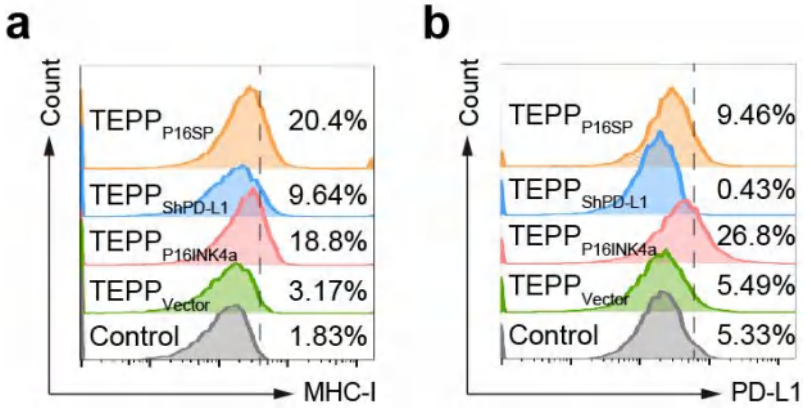

Figure S21. Representative FCM images of the surface expression of (a) MHC-I and (b) PD-L1 molecules on 4T1 cells after different treatments.

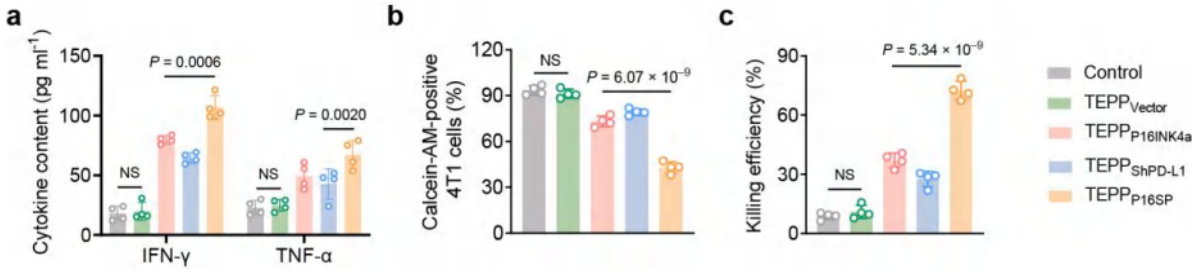

Figure S22. After T cell-mediated killing of 4T1 cells with different treatments, (a) the levels of IFN-γ and TNF-α cytokines in the supernatant were measured by ELISA, (b) quantitative analysis of calcein-AM-positive 4T1 cells was performed using FCM, and (c) killing efficiency was evaluated based on LDH release in the supernatant. $n = 4$ independent samples. Data in (a, b, c) are presented as mean ± s.d. *P* values were determined by two-way ANOVA with Tukey's post hoc corrections (a), one-way ANOVA with Tukey's post hoc corrections (b, c).

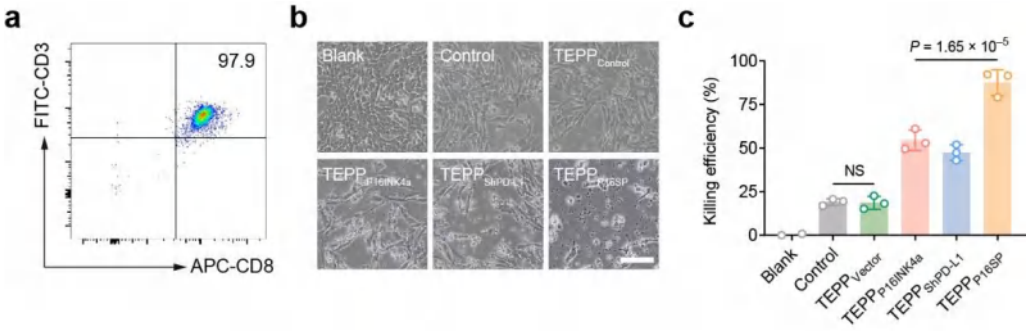

Figure S23. (a) Representative FCM images of OT-1 $CD8^+$ T cells. (b) Microscopic images of OT-1 $CD8^+$ T cells co-incubated with B16-OVA cells after different treatments at an E:T ratio of 1:1 for 12 h. (c) Quantification of cytotoxic activity using the LDH release assay. Scale bar, 50 μm. In the Blank group, E:T = 0:1. n = 3 independent samples. Data in (c) are presented as mean ± s.d. P values were determined by one-way ANOVA with Tukey's post hoc corrections (c).

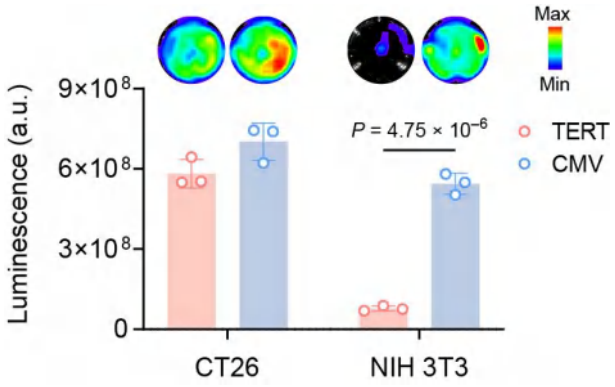

Figure S24. Transfection efficiency of TEPP in CT26 and NIH 3T3 cells. Transfection efficiency was evaluated 48 h after transfection using the pcDNA3.1-TERT-Luciferase and pcDNA3.1-CMV-Luciferase plasmids. n = 3 independent samples. Data are presented as mean ± s.d. P values were determined by two-way ANOVA with Bonferroni's post hoc corrections.

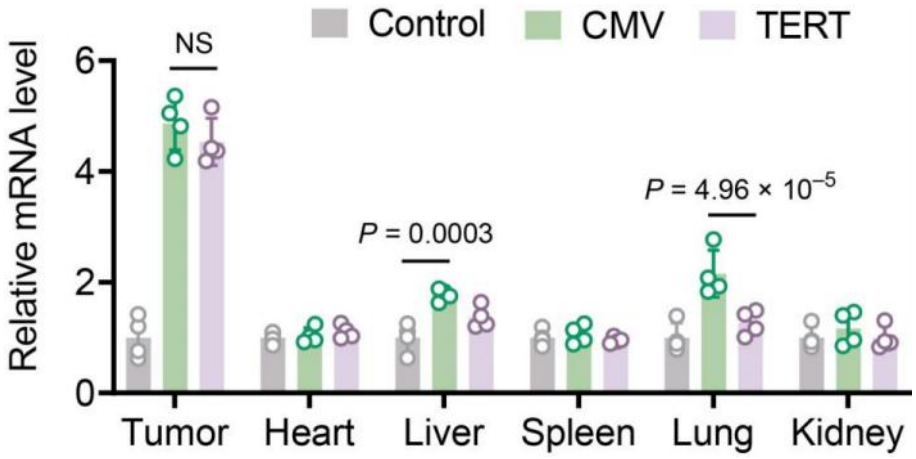

Figure S25. Quantification of $P16^{INK4a}$ mRNA expression levels in tumors and major organs after different treatments by qRT-PCR. n = 4 independent samples. Data are presented as mean ± s.d. P values were determined by two-way ANOVA with Tukey's post hoc corrections.

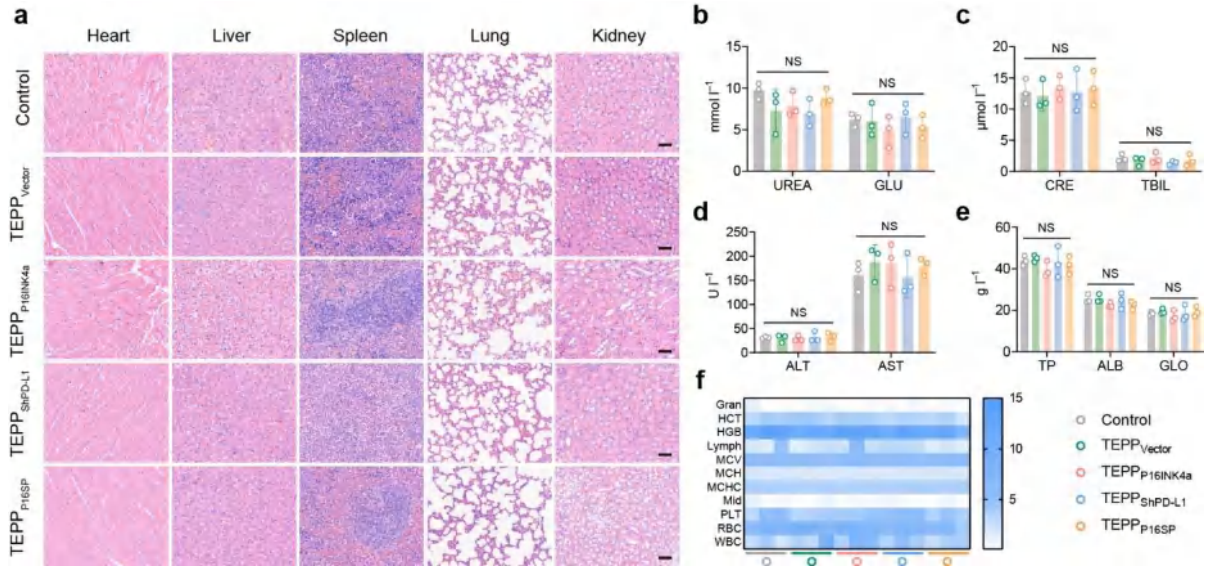

Figure S26. (a) Representative images of H&E staining of major organs from TNBC mice after different treatments. Scale bar, 50 μm. (b,c) Comprehensive blood biochemical analysis of TNBC mice at the end of treatment. Kidney function indicators, including urea (UREA), glucose (GLU), creatinine (CRE), and total bilirubin (TBIL). (d) Liver function markers, specifically alanine transaminase (ALT) and aspartate transaminase (AST). (e) Protein profile parameters, encompassing total protein (TP), albumin (ALB), and globulin (GLO). n = 3 independent samples. (f) Complete blood count analysis of TNBC mice at the end of treatment. Indicators including granulocytes (Gran, 10^9 cells l^{-1}), hematocrit (HCT, %), hemoglobin (HGB, g l^{-1}), lymphocytes (Lymph, 10^9 cells l^{-1}), mean corpuscular volume (MCV, fl), mean corpuscular hemoglobin (MCH, pg), mean corpuscular hemoglobin concentration (MCHC, g l^{-1}), intermediate cells (Mid, 10^9 cells l^{-1}), platelets (PLT, 10^9 cells l^{-1}), red blood cells (RBC, 10^{12} cells l^{-1}) and white blood cells (WBC, 10^9 cells l^{-1}). n = 3 independent samples. Data in (b-e) are presented as mean ± s.d. P values were determined by two-way ANOVA with Tukey's post hoc corrections (b-e).

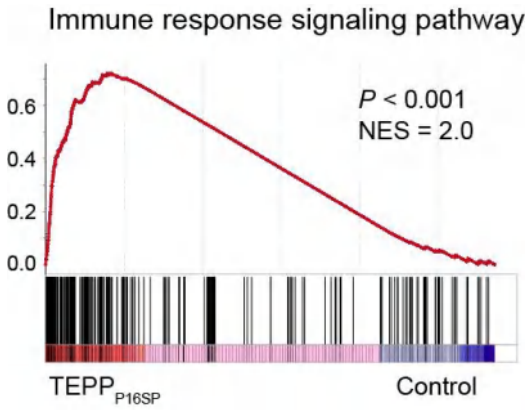

Figure S27. GSEA pathway analysis of the immune response signaling pathways associated with DEGs between the control group and the $TEPP_{P16SP}$ treatment group. *P* values were determined by permutation test.

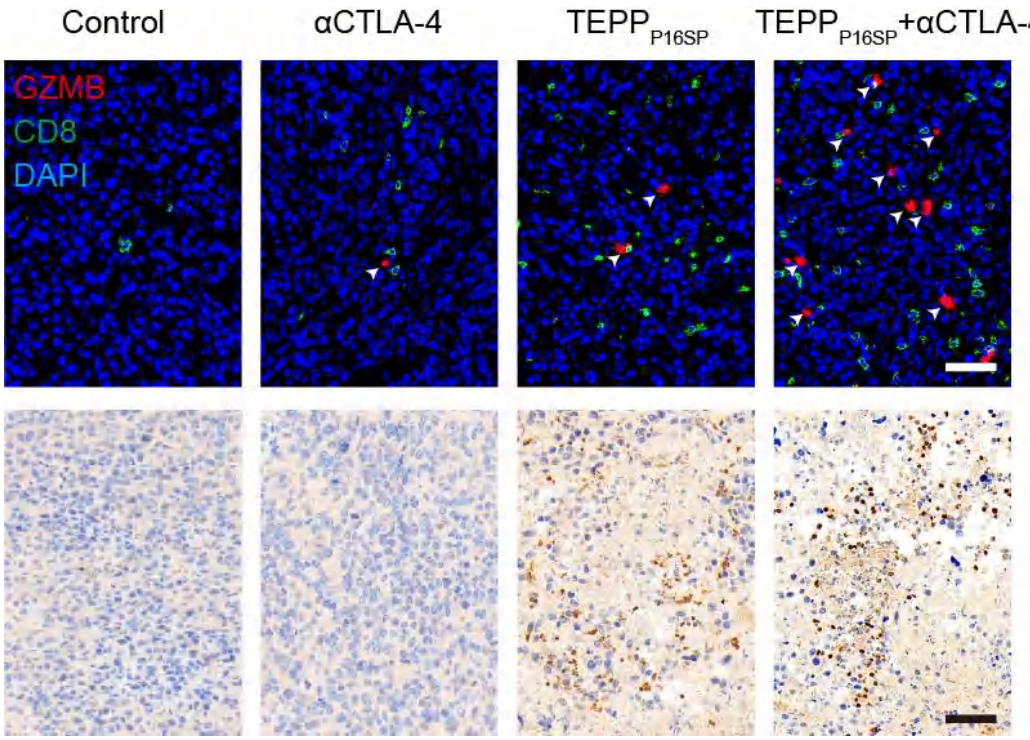

Figure S28. Representative images of immunofluorescence staining for GZMB and CD8 (top), and immunohistochemical staining for $P16^{INK4a}$ (bottom) in tumor tissues from TNBC mice after different treatments. The arrows indicate areas of GZMB secretion. Scale bar, 50 μm.

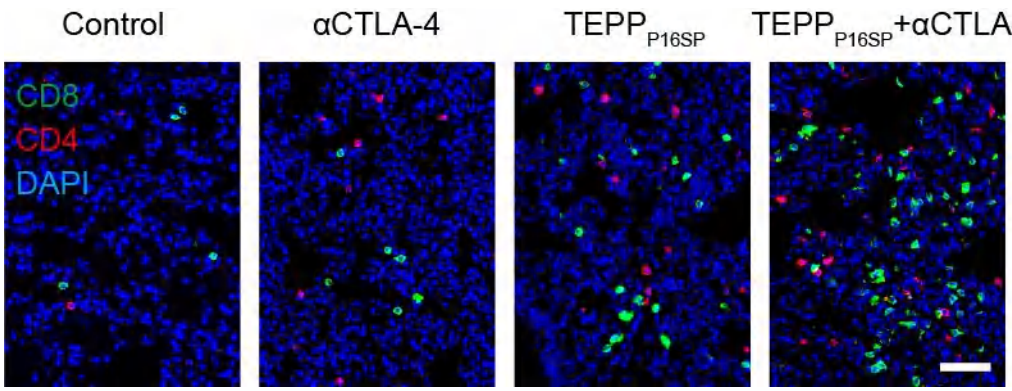

Figure S29. Representative immunofluorescence staining of CD8 and CD4 in lung metastases from TNBC-bearing mice in different treatment groups. Scale bar, 50 μm.

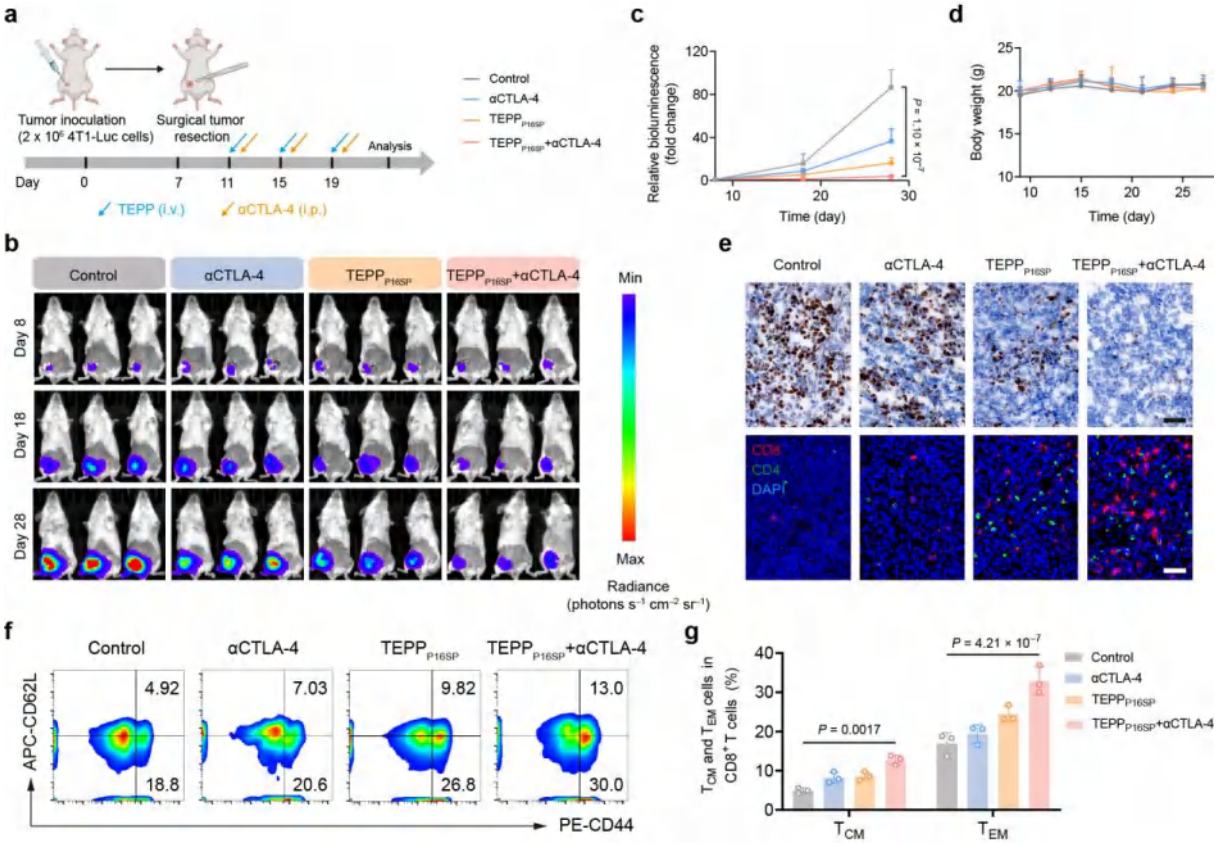

Figure S30. (a) Schematic illustration of the establishment of the TNBC postoperative recurrence model and the corresponding treatment schedule. (b) In vivo bioluminescence imaging and (c) quantitative analysis of normalized bioluminescence intensity in TNBC postoperative recurrence mice with different treatments. Three representative mice are shown for each treatment group. (d) Body weight changes of mice over a 28-day period. n = 6 independent mice. (e) Representative images of Ki67 immunohistochemical staining and immunofluorescence staining for CD4 and CD8 in tumor tissues from TNBC postoperative recurrence mice following different treatments. Scale bar, 50 μm. (f) Representative FCM plots and (g) quantitative analyses of T_{CM} and T_{EM} in spleens of TNBC postoperative recurrence mice after different treatments. n = 3 independent samples. Data in (c, d, g) are presented as mean ± s.d. P values were determined by two-way ANOVA with Tukey's post hoc corrections (c, g).

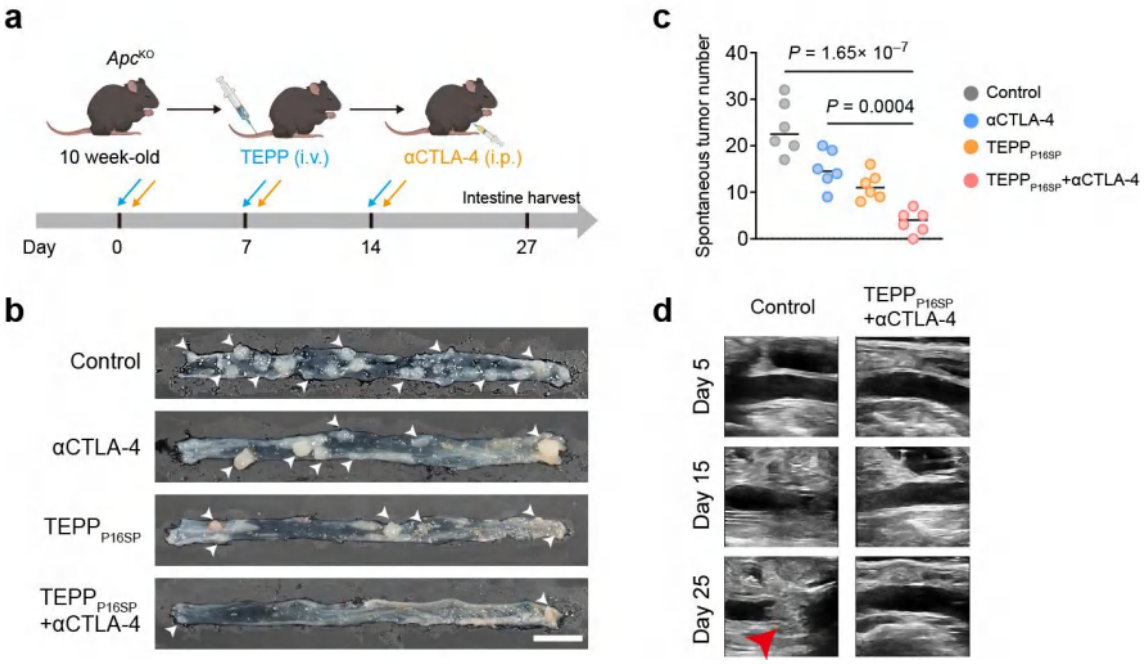

Figure S31. (a) Schematic illustration of the treatment schedule in *Apc*^{KO} models. (b) Representative intestinal images and (c) corresponding tumor counts in *Apc*^{KO} mice after different treatments. $n = 6$ independent mice. Scale bar, 1 cm. (d) In vivo US imaging of *Apc*^{KO} mice with different treatments. The red arrow indicates suspected tumor sites. *P* values were determined by one-way ANOVA with Tukey's post hoc corrections (c).

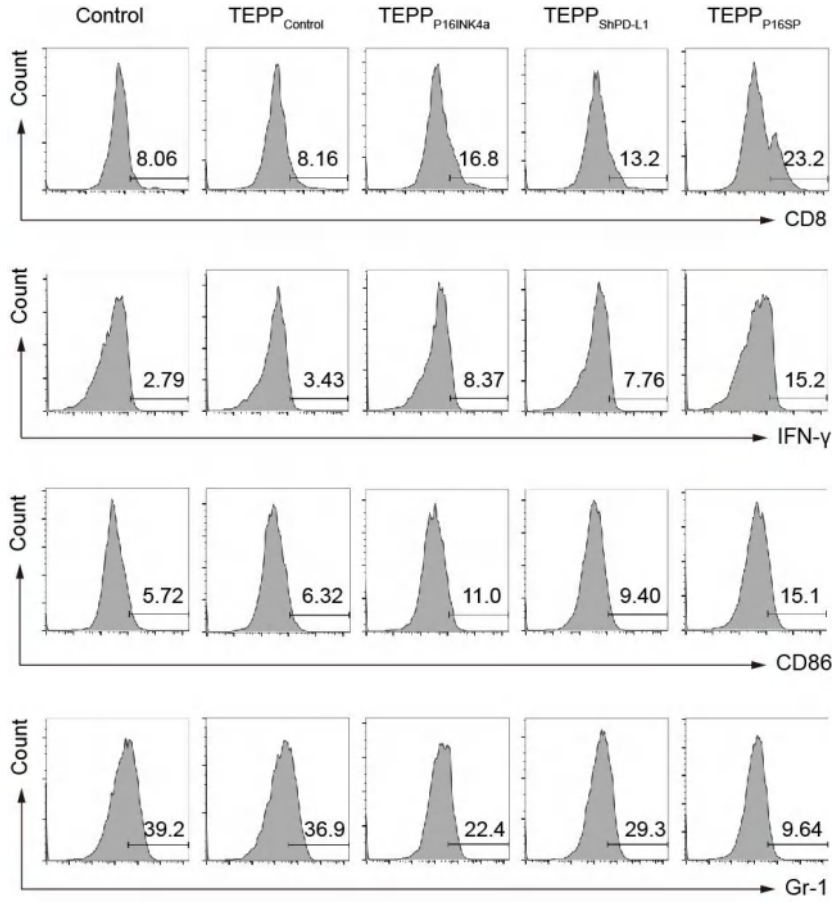

Figure S32. Representative FCM histograms of $CD8^+$ cytotoxic T cells, IFN-γ^+ $CD8^+$ T cells, M1 macrophages, and MDSCs corresponding to the data presented in Figure 5l–o.

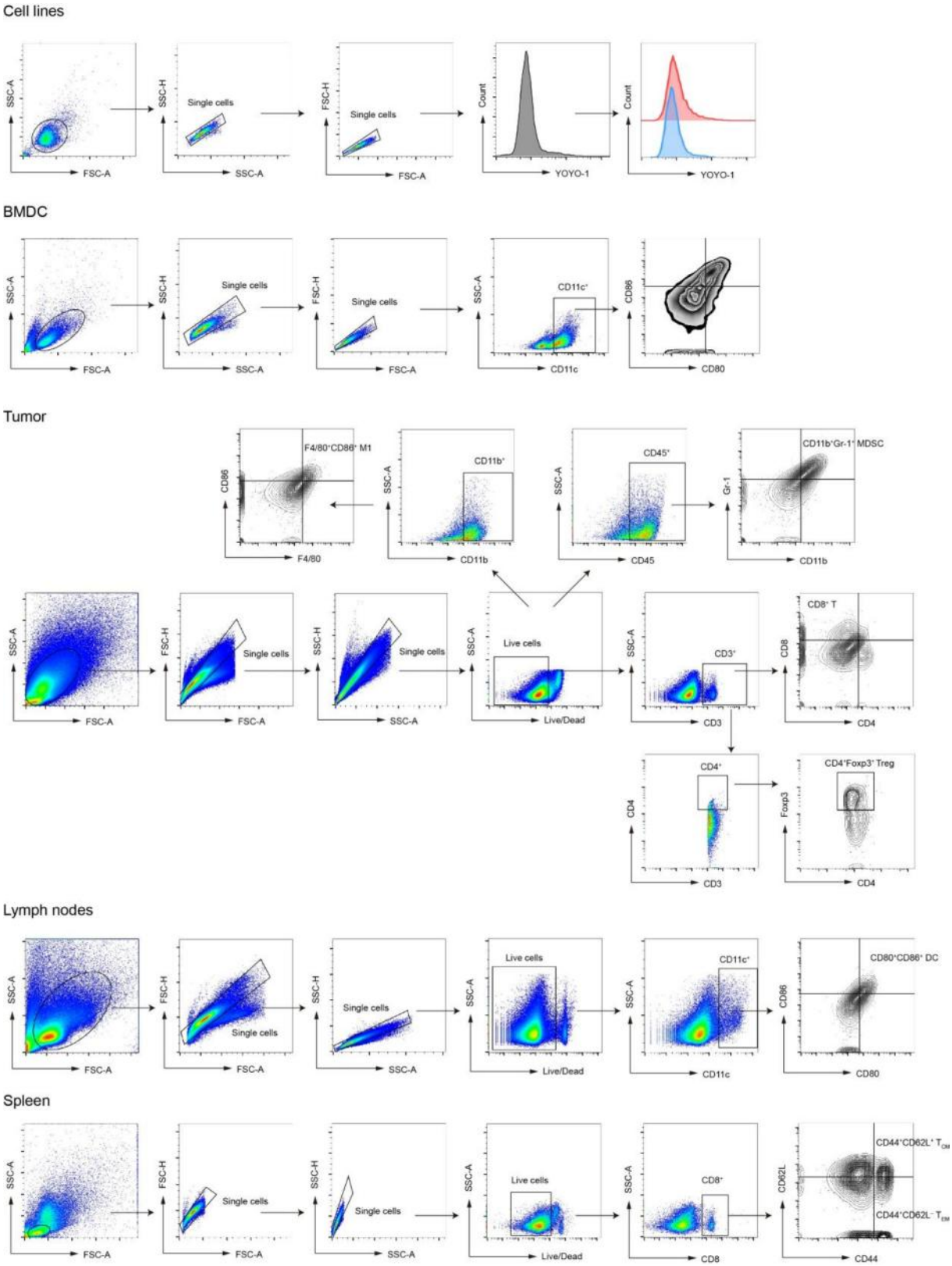

Figure S33. FCM gating strategies used for in vitro cell experiments, BMDC maturation analysis, and characterization of immune cell populations in mouse tumor tissues and immune organs.

Table S1. Coding sequence of P16^{INK4a}.

Gene name	Coding sequence
Mouse *CDKN2A*	ATGGAGTCCGCTGCAGACAGACTGGCCAGGGC GGCGGCCCAGGGCCGTGTGCATGACGTGCGGG CACTGCTGGAAGCCGGGGTTTCGCCCAACGCCC CGAACTCTTTCGGTCGTACCCCGATTCAGGTGA TGATGATGGGCAACGTTCACGTAGCAGCTCTTC TGCTCAACTACGGTGCAGATTCGAACTGCGAGG ACCCCACTACCTTCTCCCGCCCGGTGCACGACG CAGCGCGGGAAGGCTTCCTGGACACGCTGGTG GTGCTGCACGGGTCAGGGGCTCGGCTGGATGTG CGCGATGCCTGGGGTCGCCTGCCGCTCGACTTG GCCCAAGAGCGGGGACATCAAGACATCGTGCG ATATTTGCGTTCCGCTGGGTGCTCTTTGTGTTCC GCTGGGTGGTCTTTGTGTACCGCTGGGAACGTC GCCCAGACCGACGGGCATAGCTTCAGCTCAAGC ACGCCCAGGGCCCTGGAACTTCGCGGCCAATCC CAAGAGCAGAGCTAA

Table S2. ShRNA sequence of the target gene.

Gene name	ShRNA sequence
Mouse *CD274*	AAAAAAGGATATTTGCTGGCATTATACTCGAGTA TAATGCCAGCAAATATCCT

Table S3. Probe sequence for FISH experiments.

Probe name	Probe sequence (5'-3')
Plaur (uPAR)	ATACAGTGCTCTGTAGGATAGCGGCATTGC

Table S4. Primer sequences for qRT-PCR analysis.

Target locus	Forward primer (5'-3')	Reverse primer (5'-3')
Mouse-P21	CTTGTCGCTGTCTTGCACTCTG	GAAATCTGTCAGGCTGGTCTGC
Mouse-H2-K1	CGTTGCTGTTCTGGTTGTCCTT	GGGTCATGAACCATCACTTTACAAT
Mouse-Nlrc5	AGTTGGCCAAGAAGTATCTGAAG	CCTGGATGCTCACATCAATGT
Mouse-Tap1	CCATTCTCACCATAGCCAGCAC	CGAGATGTGATGGAACCTGCTG
Mouse-Il1β	GTAATGAAAGACGGCACACCC	CAGGCTTGTGCTCTGCTTGTG
Mouse-Il6	CATCCAGTTGCCTTCTTGGG	TCCAGTTTGGTAGCATCCATCA
Mouse-Il8	GGCCCAATTACTAACAGGTTCC	TGACTTCACTGGAGTCCCGTAG
Mouse-Ccl5	CGCACCTGCCTCACCATAT	TGTAGAAATACTCCTTGACGTGGG
Mouse-Cxcl10	TCCATATCGATGACGGGCC	TCTTGATGGTCTTAGATTCCGGAT
Mouse-CD274	TCACTTGCTACGGGCGTTTACT	CACTTGCTCATCTTCCTTTTCCC
Mouse-Plaur	TCGGGAATGGCAAGATGATAGA	GGTAACTCATGGTCCTGTTGGTCT
Mouse-β-actin	GTGACGTTGACATCCGTAAAGA	GTAACAGTCCGCCTAGAAGCAC
Mouse-GAPDH	CCTCGTCCCGTAGACAAAATG	TGAGGTCAATGAAGGGGTCGT

Supplementary References

[1] X. Lin, W. Chen, F. Wei, X. Xie, *Mol. Ther.* **2021**, *29*, 244.

[2] C. J. Bishop, T.-M. Ketola, S. Y. Tzeng, J. C. Sunshine, A. Urtti, H. Lemmetyinen, E. Vuorimaa-Laukkanen, M. Yliperttula, J. J. Green, *J. Am. Chem. Soc.* **2013**, *135*, 6951.

[3] T. T. Smith, S. B. Stephan, H. F. Moffett, L. E. McKnight, W. Ji, D. Reiman, E. Bonagofski, M. E. Wohlfahrt, S. P. S. Pillai, M. T. Stephan, *Nat. Nanotechnol.* **2017**, *12*, 813.